INERTIAL CONFINEMENT FUSION

TECHNICAL REVIEW

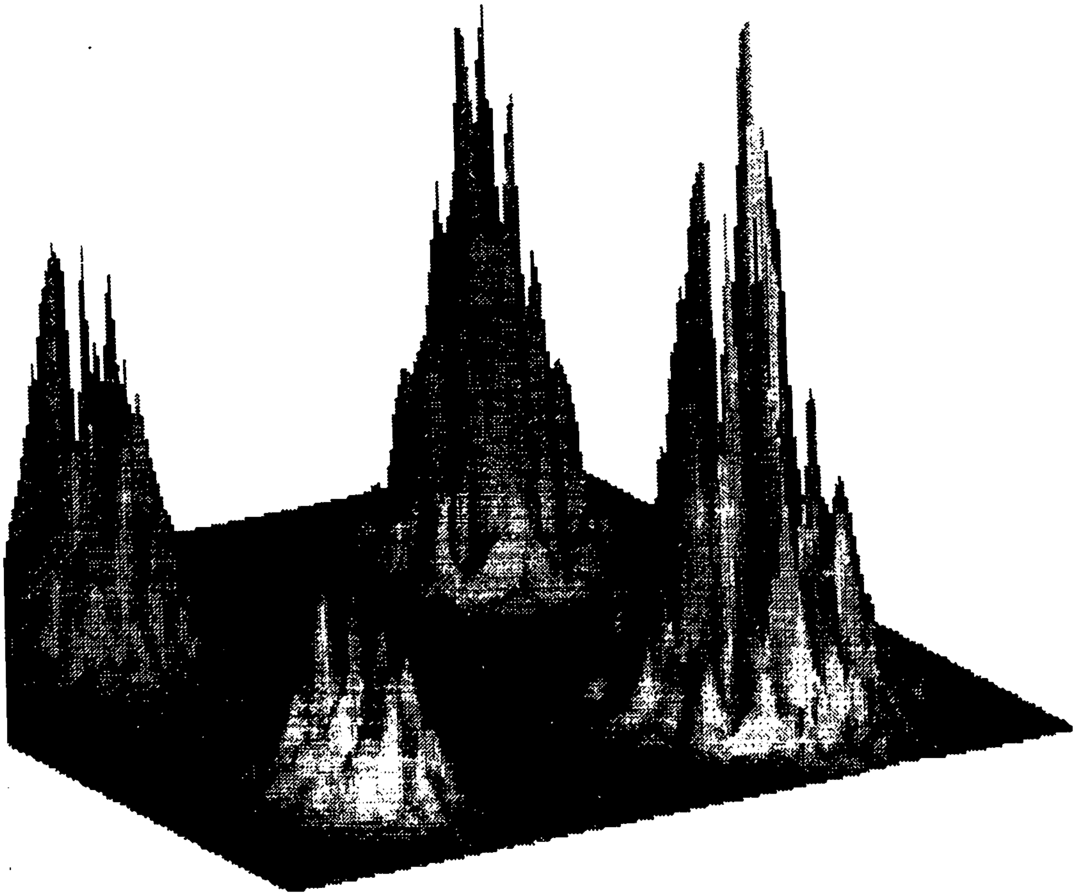

LOS ALAMOS

January 1993
Volume 2

Front Cover

Simulated GXI: Test images for symmetry legendre analysis.

Policy on ES&H

Implicit in all of our work is a respect for the health and safety of ourselves and those around us and an appreciation for the need to protect the environment in which we are privileged to work.

CONTENTS:

Technical
Review

*V*olume 2

Neutron Time-of-Flight Ion Temperature Diagnostic for Inertial Confinement Fusion Experiments

For further information
on this subject contact:

R. E. Chrien

Los Alamos
National Laboratory
Los Alamos, NM 87545

I. Introduction

Neutron time-of-flight (TOF) detectors can provide important information about the fuel-ion burn temperature in various inertial confinement fusion (ICF) target designs. Conventional current-mode neutron TOF detectors measure the time history of the total light output from many neutron interactions in a scintillator. These detectors are useful for neutron yields above 10^{10}, but are limited at lower yields by the finite emission time of the scintillator, the finite response time of the detector, and the statistics of neutron scattering and light production in the scintillator.[1]

We are constructing an ion temperature diagnostic based on individual timing measurements of single neutron interactions in many scintillators. This diagnostic is designed for low-yield targets on the Nova ICF laser facility at Livermore. The diagnostic measures the neutron arrival time distribution using an array of 960 scintillator-photomultiplier detectors with about 1-ns time resolution and operated in the single-hit mode.[2] The arrival time distribution is constructed from the results of 100 or more detector measurements. The diagnostic will be located outside the Nova target chamber at a distance of about 28 m from the target.

The ion temperature is determined from the spread in neutron energy as denoted by the relation[3] $\Delta E_n(\text{keV}) = C_{dd} T_i(\text{keV})^{1/2}$ where ΔE_n is the energy spread (FWHM) and $C_{dd} = 82.5$ (for *d-t* reactions the coefficient is $C_{dt} = 176$). The energy spread is related to the time spread by $\Delta t/t \simeq - \Delta E_n/E_n$. The quantities of interest are summarized in Table I. Corrections to the raw data must account for the system time resolution (about 1 ns) and target burn time (about 100 ps).

Table I.
Characteristics of *d-d* and d-t neutron times-of-flight for Nova

Fusion reaction	*d-d*	*d-t*
Inverse speed (ns/m)	46.1	19.2
Distance (m)	28	28
Time-of-flight (ns)	1291	538
Δt for T_i = 1 keV (ns)	21.7	3.4
1 ns distance (cm)	2.2	5.2

The neutron arrival times are detected by using a photomultiplier tube (PMT) to observe the photons produced by recoil protons in a plastic scintillator. The recoil proton energy is dependent on the proton recoil angle θ through the kinematic relation $E_p = E_n \cos^2 \theta$, where θ is measured with respect to the incident neutron direction. Since *n-p* scattering is isotropic in the center-of-mass frame, the proton recoil energy distribution is uniform up to the neutron energy. The pulse height contains no information about the incident neutron energy, but can be useful for monitoring the system gain or in some pulse pile-up rejection methods.

The dynamic range of the diagnostic covers *dd* neutron yields from 5×10^7 to 10^9. This range can be obtained through variation of the number of array channel hits (from 100 to 500) and scintillator volume (from 0.8 cm^3 down to 0.2 cm^3. Operation at yields above 10^9 can provide over-lap with results obtained from current-mode time-of-flight detectors[1] and below 5 x 10^7 with estimates of T_i obtained from first-hit analysis[1] of data from the Large Neutron Scintillator Array (LaNSA) on Nova.

Another way to extend the dynamic range is by operating the array in the multiple hit regime. An acceptable fraction (10%) of the channels will provide single hit data even when the average number of hits per channel is three. Thus a dynamic range of about 30 is possible provided that channels affected by pulse pile-up can be rejected. Data reduction based on first-hit analysis[4] can also be considered.

The detectors are enclosed in a cylindrical steel chamber (Fig. 1) which provides magnetic shielding for the PMTs. A total of 1020 PMTs, including spares, are supported by fore and back planes made of black nylon. A spring behind each PMT base presses each PMT against its scintillator. A silicone pad is used to improve the optical coupling. Gamma sources are included for *in situ* calibration. The chamber is supported by a stand which allows it to be rotated for alignment or maintenance.

The electronics for each channel (Fig. 2) consist of the PMT voltage divider base, a discriminator, a multiple-hit time-to-digital converter (TDC), and a gated charge-sensitive analog-to-digital converter (ADC). The multiple hit capability of the TDC is valuable for observing the gammas from neutron interactions with materials along the neutron flight path and thus to correct for timing differences between channels. ADCs can be valuable for recording the pulse height distribution of the recoil proton scintillations to monitor the overall health of the PMT array.

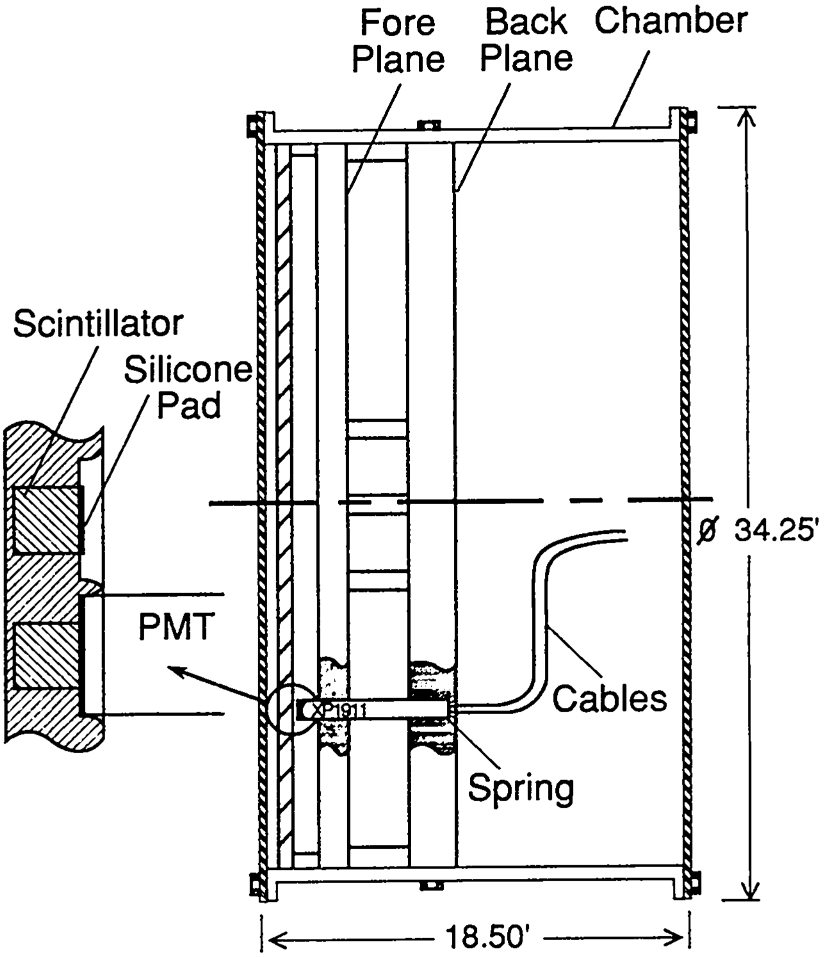

Fig. 1. Assembly drawing of the photomultiplier tube chamber, showing the scintillators, silicone coupling pads, PMTs, bases, and cables for the PMT array.

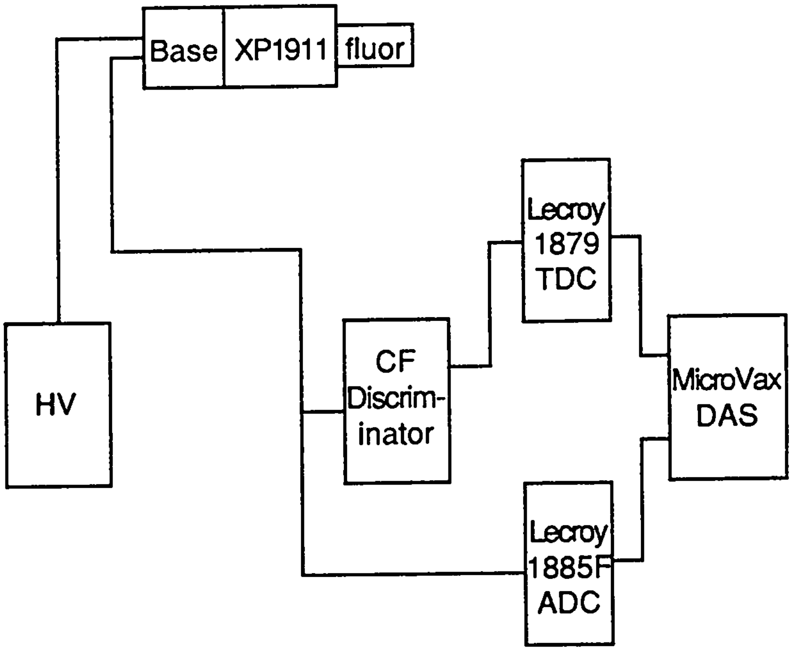

Fig. 2. Schematic of electronics for a single detector channel.

II. Scintillator

The scintillator volume is chosen to give neutron sensitivity appropriate to the yield predicted for a particular Nova shot. In all cases the scintillator thickness should be restricted to about 1 cm to keep the *d-d* neutron transit time across the scintillator less than 0.5 ns (0.2 ns for *d-t* neutrons). With the above restriction, the number of neutron interactions in each scintillator is given by $N = Y (A/4\pi R^2)(x/\lambda)$ where Y is the neutron yield, A is the detector area, R is the distance from the Nova target to the scintillator (28 m), x is the detector thickness, and λ is the neutron mean free path for elastic scattering (7.7 cm). For the minimum neutron yield of 5×10^7 and a minimum neutron number of 0.1 (to obtain 96 measurements), the scintillator volume Ax is 0.8 cm^3. For the maximum neutron yield of 1×10^9 and a maximum neutron number of 0.5, the scintillator volume drops to 0.2 cm^3. If the array is operated at a neutron number of 3, the dynamic range is increased six-fold at a given scintillator volume.

The scintillator itself should be relatively fast and bright, similar to BC400 or NE102. The light output of this scintillator is about 64% of anthracene. The light production in NE102 for electron energy deposition is 0.01 photons/eV.[5] The relative production efficiency for protons in NE102 has been measured[7] and can be expressed as $T_E = 0.95T_P - 8.0\{1 - \exp(-0.10T_P^{0.90})\}$ where T_P is the proton energy (in MeV) and T_E is the equivalent electron energy (in MeV). The light production dependence on proton energy is illustrated in Fig. 3. The number of photons varies from 110 for a 0.25 MeV recoil proton up to a maximum of 7433 for a full-energy recoil. For comparison, a full-energy recoil from *d-t* neutrons produces 80,300 photons. A

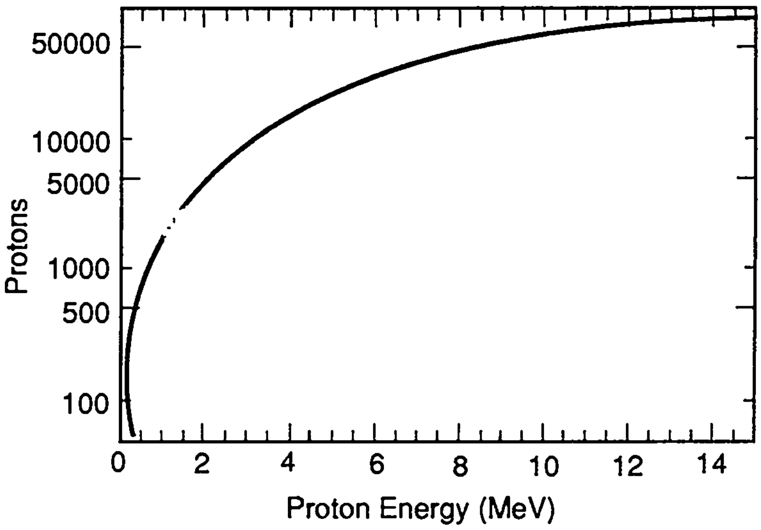

Fig. 3. Light production by protons in BC400 plastic scintillator as a function of proton energy.

useful amplitude calibration can be provided by 0.662 MeV gammas from ^{137}Cs, which produce a Compton edge at two-thirds of the recoil proton edge from *d-d* neutrons.

Light coupling efficiency can be estimated by comparing the pulse height spectra from neutron or gamma interactions in a scintillator with the single photoelectron spectrum from the PMT. Various coupling methods were evaluated using TiO_2-painted 1-cm cylindrical scintillators and a 3-cm end-viewing PMT. Coupling efficiency of about two-thirds is obtained when using optical coupling grease between the scintillator and the photocathode together with titanium dioxide paint on the uncoupled surfaces. However, the use of optical coupling grease is prohibited by the need to change the scintillators between Nova shots. Instead, silicone coupling pads can be employed. These coupling pads permit coupling efficiency close to that of coupling grease (about 50%). Bare coupling efficiency is around one-third.

III. Photomultiplier Tube

The PMT converts scintillation photons into electrons and amplifies them in the electron multiplier. Bialkali photocathodes provide a good match for plastic scintillator emission spectra and have quantum efficiency of about 25%. Thus 10-5 photoelectrons can be expected from a 0.25 MeV recoil proton. The multiplier structure should be a linear focused type to obtain good time resolution. Inexpensive side-viewing PMTs are unsuitable because of inefficient light coupling between scintillators and the recessed photocathode.

Time resolution of PMTs is quoted in terms of the single-photoelectron transit time spread (SPTTS). These SPTTS values are 2-3 ns for PMTs of the type considered. The time resolution improves inversely as the square root of the number of photoelectrons compared with the SPTTS. This dependence indicates the importance of efficient light coupling. An SPTTS of 3 ns or better is needed to obtain time resolution of 1 ns for *d-d* measurements with as few as 10 photoelectrons. Better time resolution is obtained with brighter *d-t* scintillations.

The anode output must be compatible with the discriminator threshold. Assuming a minimum of 10 photoelectrons, a gain of 10^6, and a triangular anode pulse with FWHM of 5 ns, the peak anode current is 320 μA. This represents 16 mV into a 50 Ω load, which provides a reasonable minimum voltage for the discriminators. In addition, the PMT output should remain linear up to the recoil proton edge (about 20 mA for *d-d* neutrons).

A variety of small 10-stage end-viewing PMTs were considered for this diagnostic. The Philips XP1911 19 mm tube was selected, primarily based on cost. This PMT provides the required gain (at a nominal voltage of 1600 V) and linear current (up to 130 mA).

The time resolution was measured by comparing the anode pulses from two XP1911 PMTs viewing the same scintillator (Fig. 4). Neutral density filters between the scintillator and each PMT provide an attenuation of 200, ensuring that each scintillation produces at most a single photoelectron pulse. Ortec VT120C linear preamplifiers provide an amplification of 10 for each anode signal. A 20 ns coax line was used to delay one of the signals. Ortec 473A constant-fraction discriminators and an Ortec 567 Time-to-Amplitude Converter were used to obtain the raw timing spectrum shown in Fig. 5. The time spread Δt can be expressed as $\Delta t^2 = \Delta t_A^2 + \Delta t_B^2 + \Delta t_{scin}^2$ where Δt_A and Δt_B refer to the SPTTS of the two PMTs and Δt_{scin} refers to the FWHM emission time of the scintillator (1.3 ns). For identical A and B channels, the SPTTS of each tube is 3.1 ns. Measurements with reduced neutral density filtering confirm the expected improvement of time resolution with light level.

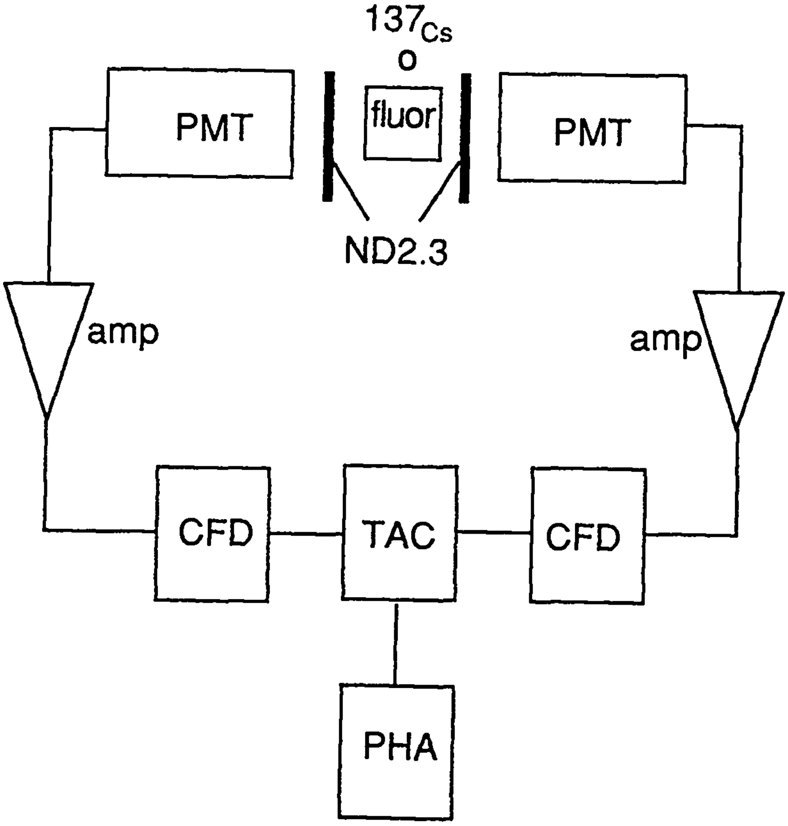

Fig. 4. Schematic of electronics used for measuring single-photoelectron transit time spread by the two photomultiplier tube method.

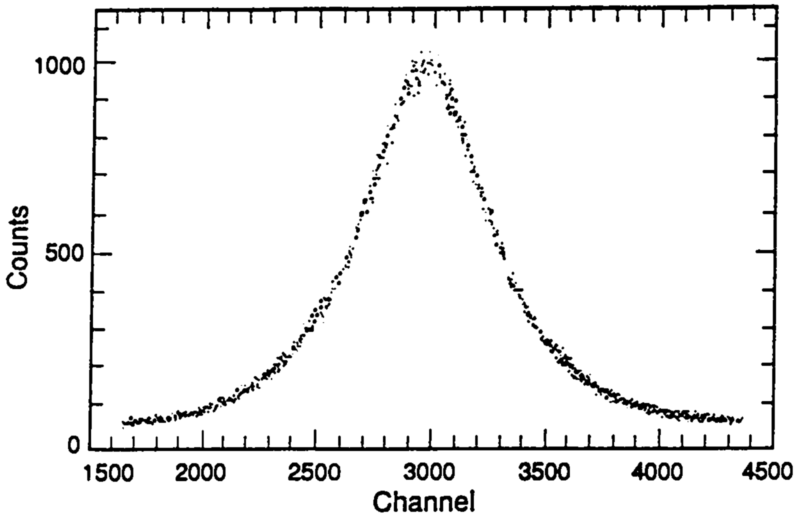

Fig. 5. Transit time spectrum obtained with the two photomultiplier tube method using XP1911 tubes and a BC418 scintillator. The calibration factor is 155 channels per ns. The full width at half maximum corresponds to 4.5 ns.

The PMT voltage divider is conservatively designed for bleeder current equal to the average anode current rating of the tube. The manufacturer's recommended string for maximum linear current output is employed. Capacitive stabilization of the latter dynode stages is provided to limit voltage changes to less than 1% for 10 full-energy proton recoil scintillations. Positive high voltage is supplied to the anode to permit the cathode region to be grounded. Anode output is capacitively coupled to the discriminator.

IV. Discriminator, ADC, TDC, and Data Acquisition

The anode signals are connected to novel constant-fraction-like discriminators based on a simple RC network and a fast voltage comparator.[7] No walk correction is required with this discriminator. An updating output of 10 ns minimum duration is provided to allow pulse pile-up to be detected by the TDC. This discriminator has low power dissipation and can be made quite compact.

The discriminator provides a buffered version of the anode signal for connecting to a LeCroy 1885F 15-bit charge ADC. This is a 96 channel

FASTBUS module. The 1885F can be gated for a time as short as 50 ns and can be used to measure the amplitude of the *d-d* neutron pulses with a sensitivity of 50 fC per count.

The discriminator output is connected to LeCroy 1879 96-channel multihit TDC FASTBUS modules. These are 2 ns TDCs with double-edge resolution of 10 ns. Up to 16 edge timing measurements per channel can be obtained. For *d-t* measurements, the TDCs will be upgraded to the 0.5-ns LeCroy 1877 when that product becomes available.

A DEC MicroVax II computer is used to control and read out the FASTBUS modules and to analyze the data. A CAMAC-based Starburst LSI-11 mediates the control functions through a CAMAC-FASTBUS interface. The software needed for this diagnostic has already been developed for the LaNSA array.

V. Testing

The two general areas of testing are amplitude and timing tests. The overall gain of the scintillator-PMT system must be monitored routinely, perhaps prior to each Nova shot, and the PMT voltage or discriminator threshold adjusted to correct for gain shifts or changes in PMT coupling efficiency. Small ^{137}Cs radioactive sources are used for this calibration. Timing tests will be performed using a 1-ns, blue, unfocused CRT light pulser developed at EG&G.

Once in operation, correct system performance will be checked by monitoring the recorded data. Timing can be routinely checked by observing x-ray generating targets or by using the gamma fiducial provided by neutron interations in the target. Spare channels are included in the array.

PMT failures can be discovered by detecting a change in the divider string current, the appearance of excessive noise, or by the absence of signal in a particular channel for a series of shots. Discriminator and TDC problems will be detected by comparing the average detection probability in each channel with the average detection probability in the whole array. An overall alignment check can be performed by computing the average arrival time as a function of two orthogonal dimensions across the detector array. Individual channel timing variations can also be detected by comparison with the average arrival time.

IV. Acknowledgement

This work was done in collaboration with David F. Simmons and Dale L. Holmberg, EG&G Energy Measurements, Las Vegas, Nevada.

Radiation Field Effects on the Spectroscopic Properties of C1 and Fe Seeded Plasmas

For further information
on this subject contact:

J. Abdallah, Jr.,

R. E. H. Clark

Los Alamos
National Laboratory
Los Alamos, NM 87545

I. Introduction

Comparisons of theoretical spectral simulations and experimental observations often provide useful information concerning the state of a laboratory plasma. The electron temperature and density can be estimated from various spectral features, i.e., line ratios, line widths, background continuum, comparison with synthetic spectra, etc. These techniques are useful for a variety of applications including magnetic fusion, inertial confinement fusion, opacity determination, x-ray lasers, and astrophysics. These methods are discussed at length in several articles.[1-6]

The calculation of accurate ionization balance and level populations is of fundamental importance to any spectral simulation. Populations can be calculated using a variety of methods whose validity depends upon plasma conditions. Coronal equilibrium, in which ions exist in ground states only, is valid at low electron densities depending on the element.[3] Local thermodynamic equilibrium (LTE) is valid at high electron densities, or when radiation is in equilibrium with thermal electrons. Collisional-radiative steady-state which include excited states explicitly bridge the gap between coronal equilibrium and LTE. Time dependent kinetics is required for transient plasmas. The calculation of level populations is also directly dependent on the energy levels and cross sections that are used to describe the atomic processes which occur. These control the rate of population and depopulation of individual atomic levels.

In principle, the coronal and collisional-radiative treatments should include radiation effects when fields are present. Photon induced processes should be accounted for in the rate equations. However, usually only electron collisions and spontaneous process are considered. The radiation field introduces a competition between electrons and photons for atomic excitation and ionization processes. The competition varies as a function of electron density, electron temperature, and the applied radiation field strength.

The purpose of the current work is to assess the effect of an intense background radiation field on the spectroscopic properties of a plasma as a function of electron temperature, density, and radiation temperature. A steady-state kinetics approach is used. Plasma conditions are chosen such that K-shell emissions from Cl and Fe ions with 1-3 bound electrons are prevalent. The radiation field is taken to be black body with temperatures of several hundred electron volts.

The effect of radiation on various line ratios will be studied. Line ratios are intensity ratios of one line to another as a function of electron density and temperature. Line ratios are useful because they can provide a rough diagnostic of plasma conditions without a complete analysis of a complicated spectrum. They also provide insight into the various processes which drive transitions.

The computational method will be discussed in Sec. II, results will be discussed in Sec. III, and conclusions will be presented in Sec. IV.

II. Computational Method

The kinetic approach used here has been applied previously.[7] The net production rate of level p of ion stage i is given by

$$\frac{dN_{ip}}{dt} = F_{ip}\left(\{N_{jq}\}, N_e, T_e, T_r\right) \ , \qquad (1)$$

where N_{ip} is the number density of ions in level p of ionicity i ($i = 1$ represents the neutral atom, $i = 2$ represents the singly charged species, etc.), τ is time, $\{N_{jq}\}$ represents the set of all levels that are involved in reactions with level ip, N_e is the electron density, T_e is the temperature which describes the electron energy distribution through the Maxwellian function, and T_r is the radiation temperature that describes the photon energy distribution through the Planckian black body function. Electron and photon distributions are restricted to Maxwellians and Planckians, respectively, for the purpose of this paper. The function F has the form

$$F_{ip} = \sum_{\alpha jq} N_{jq} Q_{\alpha jqip} - \sum_{\alpha jq} N_{iq} Q_{\alpha ipjq} \ , \qquad (2)$$

where the first sum contains the contributions from all processes which populate level ip, and the second sum contains the contribution from all processes which depopulate level ip. $Q_{\alpha ipjq}$ represents the rate coefficient for process α which act on an ion in level ip and leaves it in a final level jq. The rate coefficient is essentially the integrated cross section for a process weighted by the appropriate electron or photon distribution function. The Q's include the appropriate factors of N_e for processes initiated by electron collisions. They also depend on T_e for processes initiated by electron collisions, T_r for processes initiated by photon collisions, and on both T_e and T_r for processes like stimulated radiative recombination which involve both photons and free electrons. Rate coefficients are independent of distribution functions for spontaneous processes such as autoionization and spontaneous emission. Other processes, such as ion-ion collisions are beyond the scope of the present paper.

The steady-state, or large time constant population solution of Eq. (1) is given by

$$F_{ip} = 0 \ . \tag{3}$$

If the free electron density N_e is specified then Eq. (3) forms a system of linear algebraic equations which is solved assuming charge conservation, that is,

$$\sum_{jq} (j-1) N_{jq} = N_e \ . \tag{4}$$

The resulting set of N_{jq} may then be renormalized to any desired total ion density N.

The solution of Eq. (3) provides level populations for given N_e, T_e, and T_r. These level populations may then be used to predict the spectroscopic properties of the plasma. For example, the intensity of a spectral line may be expressed as[8]

$$I_{ipq} = N_{ip} A_{ipq} E_{ipq} \ , \tag{5}$$

where N_{ip} represents the population of level ip, A_{ipq} is the Einstein A coefficient for spontaneous emission from level ip to level iq, and E_{ipq} is the energy separation between levels ip and iq. The quantities A_{ipq} and E_{ipq} are readily available from the atomic physics data and they are independent of N_e,T_e, and T_r. It is often useful to form line ratios,

$$R_{ipquv} = I_{ipq} / I_{juv} \ , \tag{6}$$

which give the relative intensity of one line relative to another. Hence, a line ratio can be extracted from an experimental measurement and compared to theoretical predictions to estimate the plasma conditions. A ratio which is approximately independent of electron density is a good temperature indicator, and vice versa.

The processes included in Eq. (3) for the present study are photoexcitation, spontaneous decay, stimulated decay, electron collisional excitation, and de-excitation, photoionization, radiative recombination, stimulated radiative recombination, collisional ionization, three body recombination, autoionization, and dielectronic recombination. The cross sections for excitation and ionization are evaluated from the detailed atomic physics calculations discussed below. The rate coefficients for the reverse reactions are calculated using the principle of detailed balance. For $T_r = 0$, the rate coefficients for photoexcitation, photoionization, and the contributions due to stimulated decay and stimulated radiative recombination are zero. All processes are followed individually, therefore, no net effective rate coefficients are introduced. For example, inner shell excitation, autoionization, and radiative decay are all included as separate processes.

Table I summarizes the electron configurations which were used to model each of the ion stages included in the kinetics. Note that the calculations have been restricted to the Be-like, Li-like, He-like, and H-like ion stages, since those are the ions of interest for the density and temperature domain of the current study. Detailed atomic structure calculations using the method of Cowan[9,10] were performed to generate the set of fine structure energy levels corresponding to the configurations of Table I. The structure calculations include

Table 1

Be-like	$1s^2[2s2p]^2$ $1s[2s2p]^3$	
Li-like	$1s^2[nl]$ $1s[2s2p]^1nl$	$2\ n\ 5$
He-like	$1s[nl]^1$ $[2s2p]^2$	$2\ n\ 5$
H-like	$[nl]^1$	$1\ n\ 5$

Configurations used to generate the level structure for each of the ion stages included in the atomic model. The notation $[\ ]^w$ means all possible distributions of w electrons in the shells specified inside the brackets. All possible allowed values of the orbital angular momentum quantum 1 are included.

spinorbit coupling and configuration interaction. Each resulting level is denoted by total orbital angular momentum L, total spin S, and total angular momentum J. The energy levels and wave functions produced by these calculations are used consistently to generate the required cross sections.

Oscillator strengths were calculated for all possible level-to-level dipole allowed transitions. The oscillator strengths are used to evaluate the radiative excitation and de-excitation rate coefficients. Plane-Wave-Born (PWB) collision strengths9 were calculated for all possible pairs of level-to-level transitions. These strengths are used to calculate rate coefficients for electron collisional excitation and de-excitation. Distorted wave (DW) collision strengths were calculated[11] for the most important transitions. These include all $1s \rightarrow nl$ in the H-like ion, all $1s^2 \rightarrow 1snl$ and $1s2l \rightarrow 1s2l'$ in the He-like ion and all $1s^22l \rightarrow 1s^22\ l'$, $1s^22l \rightarrow 1s2l2l'$, and $1s2l2l' \rightarrow 1s2l2l''$ in the Li-like ion. The more accurate DW cross sections are required to yield more reliable spectroscopic results.

Photoionization and autoionization cross sections were calculated for all possible level-to-level transitions between adjacent ion stages using the atomic structure wave functions discussed above. Level-to-level collisional ionization cross sections were calculated using the calculated fine structure energies and fits to scaled hydrogenic theory.[12]

III. Results and Comparisons

The methods described in the previous section were applied to chlorine and iron seeded plasmas. The effect of varying radiation fields on level populations was studied by examining the ionization balance and assorted line ratios as functions of electron temperature and/or density. Results were randomly checked using the RATION code[8] which were in general agreement with the present calculations (this code uses less detailed atomic physics).

A. Ionization Balance

Figures (1a-d) show the ionization balance for chlorine as a function of electron temperature for electron densities of 10^{19}, 10^{20}, 10^{21}, and 10^{22} cm^{-3}, respectively. Each figure shows the ionization balance for $T_r = 0$, 200, and 300 eV. The fraction for an ion species i is given by

$$f_i = \sum_q (N_{iq}/N) \ . \qquad (7)$$

The figures show that the ionization balance for low T_r is not very sensitive to N_e and that the largest effect of radiation is at low electron densities, where photon collisions are more dominant. For example, at $N_e = 10^{19}$ cm^{-3}, the 300-eV radiation

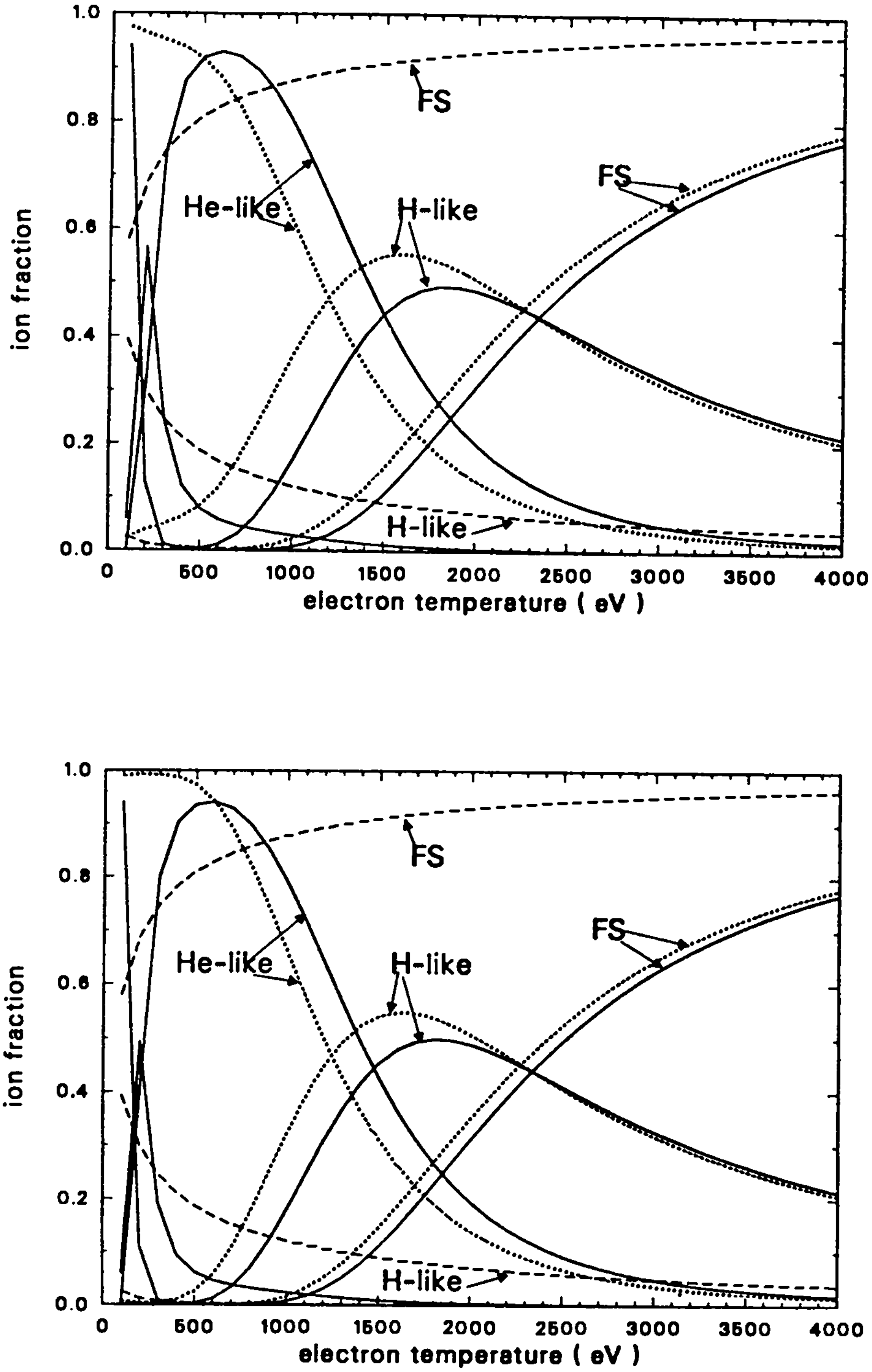

Fig. 1 Ion fraction as a function of electron temperature for various cases, 1-a through 1-d correspond to chlorine at electrodensities of 10^{19}, 10^{20}, 10^{21}, and 10^{22} cm^{-3}, and 1-e corresponds to iron at an electron density of 10^{19} cm^{-3}. The solid line corresponds to $T_r = 0$ eV, the dotted line corresponds to $T_r = 200$ eV, and the dashed line corresponds to $T_r = 300$ eV. The curves labeled by FS correspond to the tally stripped bare nucleus.

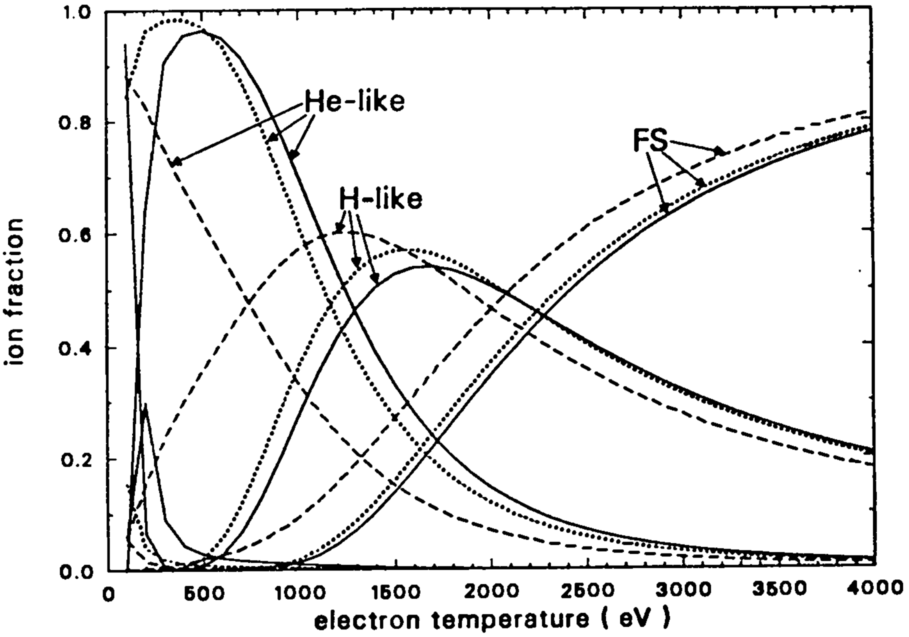
1.0
0.8
0.6
0.4
0.2
0.0
ion fraction
0
500
1000
1500
2000
2500
3000
3500
4000
electron temperature (eV)
He-like
H-like
FS

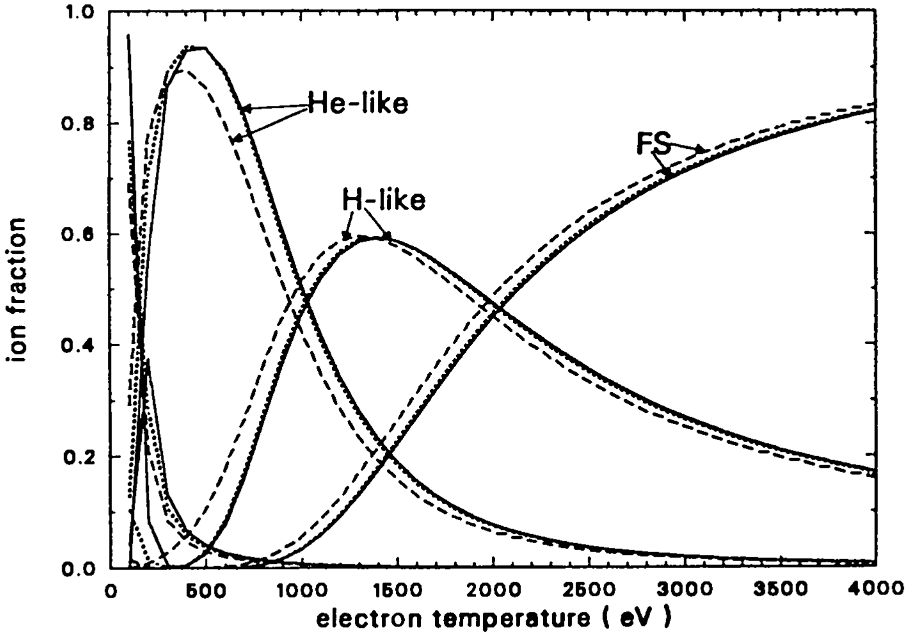
1.0
0.8
0.6
0.4
0.2
0.0
ion fraction
0
500
1000
1500
2000
2500
3000
3500
4000
electron temperature (eV)
He-like
H-like
FS

field strips most chlorine nuclei of all bound electrons. As N_e is increased, electron collisions become more dominant, and the ionization balance approaches the $T_r = 0$ result. At $N_e = 10^{22}$, the T_r = 200-eV ionization balance is essentially the same as the $T_r = 0$ result. Also note that the stronger radiation fields produce more ionization, as expected. Figure 1e shows the effect of radiation on ionization balance for iron at $N_e = 10^{19}\ cm^{-3}$. The figure shows that the radiation is ineffective for ionizing the K-shell electrons of iron, which have a larger binding energy than chlorine. The figure also shows that the He-like ion stage dominates over most of the temperature range. As electron density is increased (not shown), the $T_r > 0$ ionization balance approaches the $T_r = 0$ result, just as in chlorine.

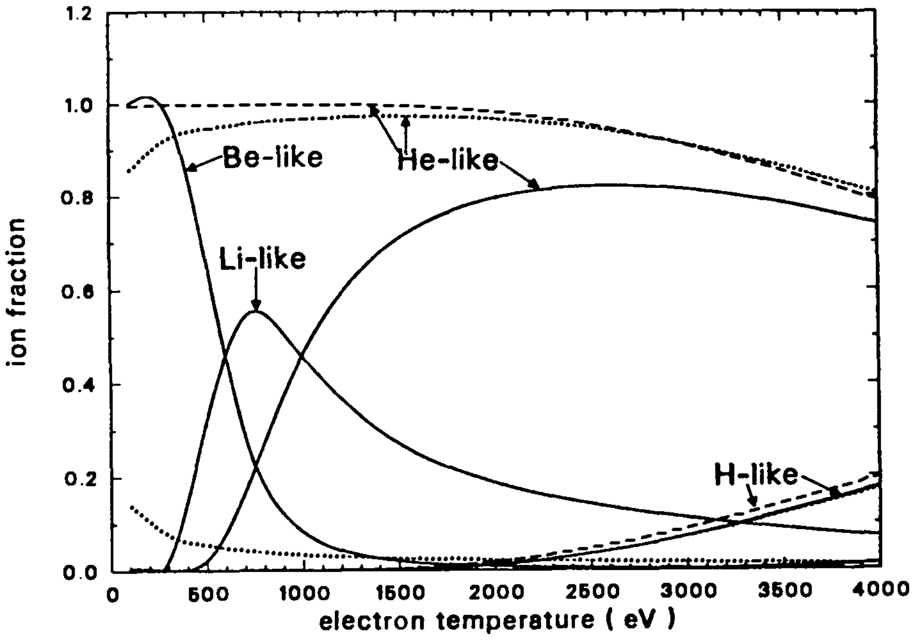

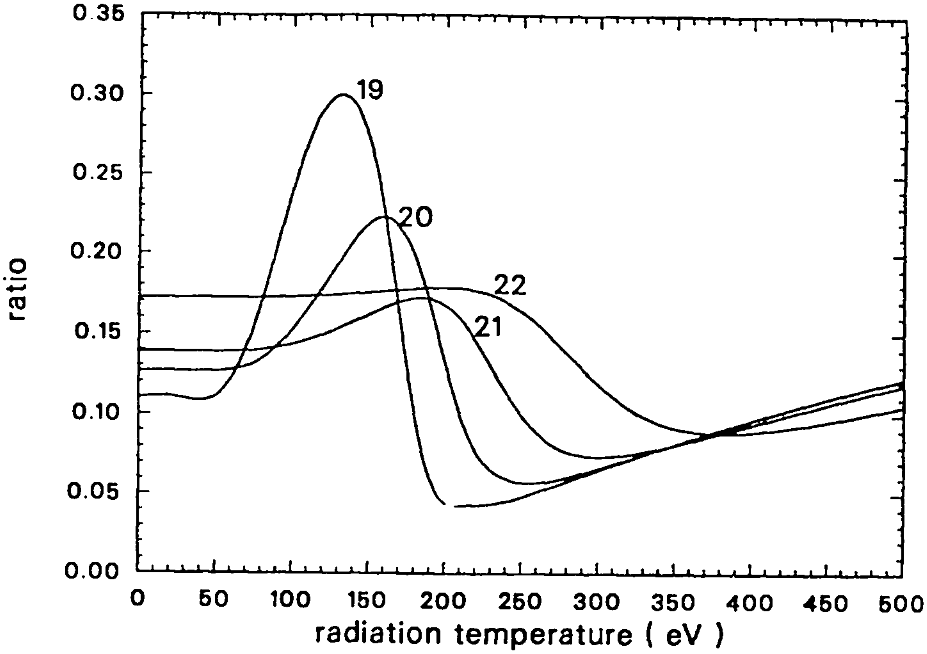

Fig. 2. The 3-1/2-1 line ratio of He-like chlorine as a function of radiation temperature for various electron densities at an electron temperature of 1000 eV. The curves are labeled by $log_{10} N_e$.

B. Electron Temperature Sensitive Line Ratios

Figure 2 shows the effect of radiation on the $1s3p\ ^1P_1$ - $1s^2\ ^1S_0/1s2p\ ^1P_1$ - $1s^2\ ^1S_0$ (3-1/2-1) line ratio of He-like chlorine (Cl XVI) for various densities at $T_e = 1000$ eV. This ratio is mildly sensitive to electron temperature and provides useful information about the populations of different n levels for the same ion stage. The ratios start out constant at values of T_r near zero. At low electron density, as the radiation temperature is increased, the manifold of $n = 2$ to $n = 3$ transitions are pumped by photons and cause the ratio to increase by a factor of 3. The ratio begins to drop as $n = 1$ to $n = 2$ transitions from the ground state become possible. As the radiation temperature increases even further, the ratio begins to increase again due to direct excitation from $n = 1$ to $n = 3$. As electron density increases, higher radiation temperatures must be attained to obtain these excitations because of increased photon-electron competition, and the curves are displaced toward the right. Also note that the variation of the curves decreases with increasing density. At $N_e = 10^{22}$, the effect $n = 2$ to $n = 3$ photo-pumping is negligible. Figure 3 shows the results for iron under the same conditions as Fig. 2. The Fe curves are displaced toward higher radiation temperatures than in the chlorine case because of larger energy level separations.

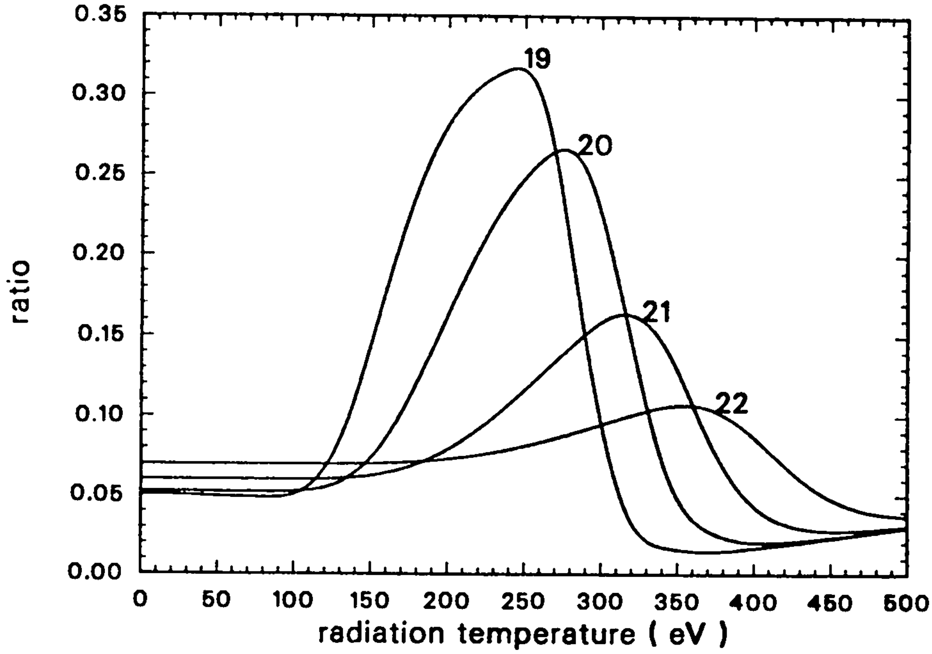

Fig. 3. The 3-1/2-1 line ratio of He-like iron as a function of radiation temperature for various electron densities at an electron temperature of 1000 eV. The curves are labeled by $\log_{10} N_e$.

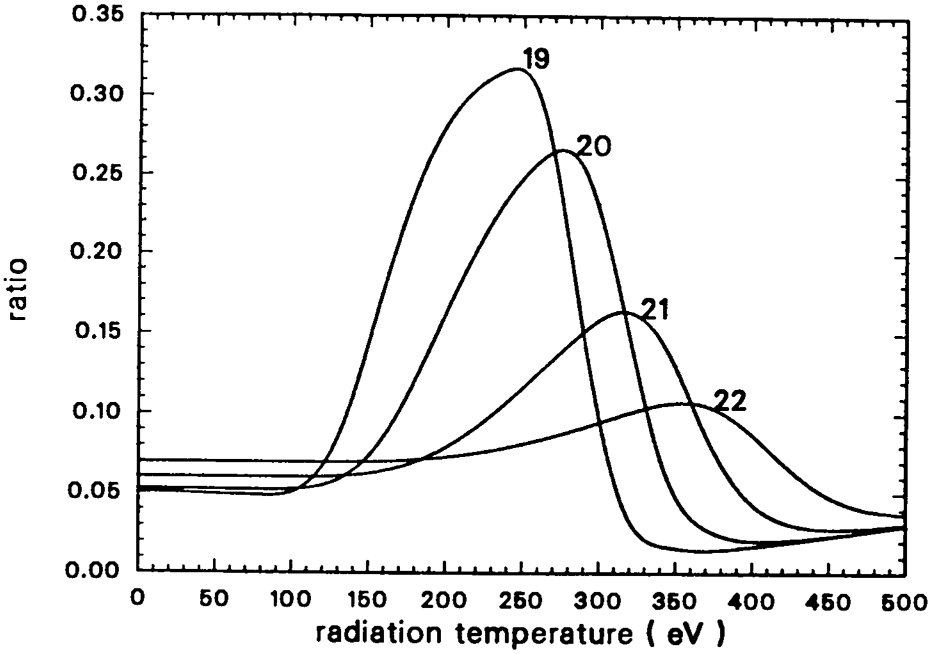

Fig. 4. The 3-1/2-1 line ratio of He-like chlorine as a function of electron temperature for various radiation temperatures at $N_e = 10^{19}$ *cm*$^{-3}$*. Each curve in labeled by the radiation temperature in eV.*

Figure 4 shows the He 3-1/2-1 ratio for chlorine as a function of electron temperature for T_r = 0, 100, 200, and 300 eV at $N_e = 10^{19}$ cm^{-3}. The driving photo-excitation processes are apparent by comparison with Fig. 2. At T_r = 300, the level populations become independent of electron temperature; indicating that photons dominate the excitation processes. Figure 5 shows the line ratio for this transition in iron at the same density. Note that the 100-eV radiation field has no effect on the level populations which is consistent with Fig. 3. As radiation temperature is increased, the population of the $n = 3$ levels are enhanced by radiation through $n = 2$ to $n = 3$ photoexcitations. The curves are strongly dependent on electron temperature because electron collisions are necessary to populate the $n = 2$ levels. Note that at even T_r = 300 eV, pumping from the ground state does not play a significant role as it did in chlorine. As electron density is increased (not shown), electron collisions become more important, and the deviation from T_r = 0 decreases. Similar results are obtained for the corresponding line ratios of the H-like ions.

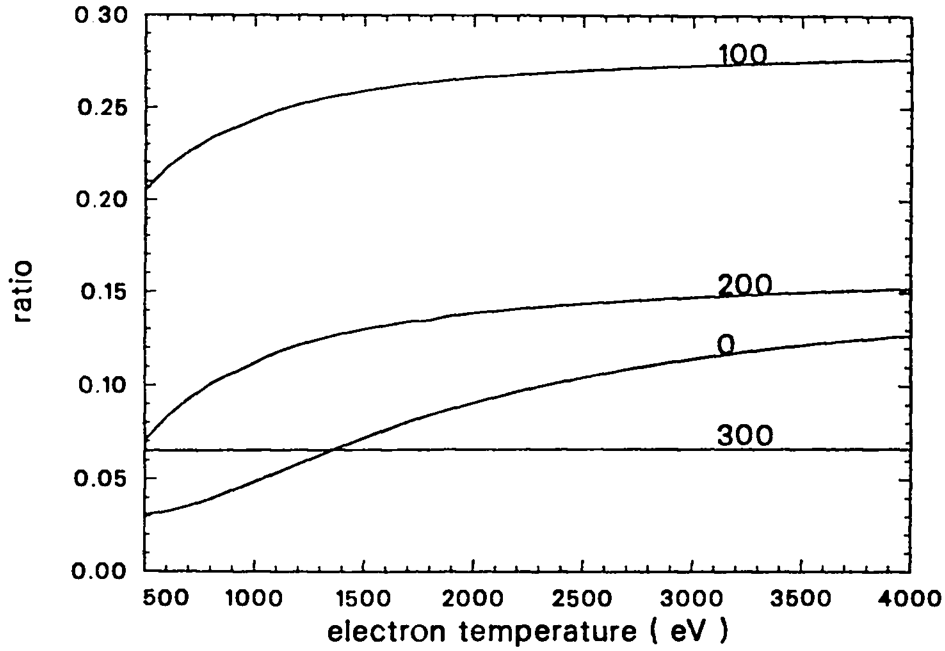

Fig. 5. The 3-1/2-1 line ratio of He-like iron as a function of electron temperature for various radiation temperatures at N_e = 10^{19} cm^{-3}. Each curve in labeled by the radiation temperature in eV.

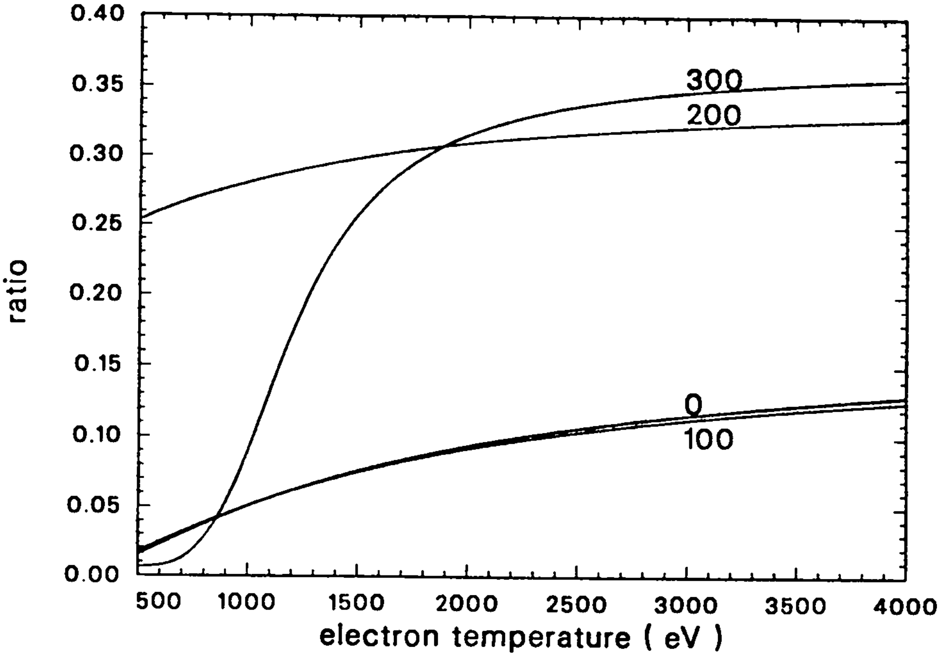

Fig. 6. The chlorine jkl/He 2-1 line ratio as a function of electron temperature at various electron densities. The solid curves correspond to $T_r = 0$ at $10^{19}, 10^{20}, 10^{21}$, and 10^{22} and are difficult to distinguish and unlabeled. The dashed curves correspond to $T_r = 200$ eV labeled by the $\log_{10} N_e$.

Figure 6 shows how a perfectly good temperature diagnostic is affected by a radiation field.[4] For this example, the $jkl/1s2p\ ^1P_1$ - $1s^2\ ^1S_0$ (jkl/He 2-1) line ratio of Cl is considered. The notation jkl is used to specify the $1s2p^2\ ^2D$ - $1s^22p\ ^2P$ transition of the Li-like ion. The four solid curves represent the line ratios at $10^{19}, 10^{20}, 10^{21}$, and 10^{22} cm^{-3} with $T_r = 0$. Note that these curves are essentially independent of electron density, all of them practically lay on top of each other and hence provide an excellent temperature diagnostic. When a 200-eV radiation field (dashes, curves) is applied the curves become nondegenerate. This is caused by photo-pumping of the $n = 2$ level by the radiation field. The effect is greatest for low electron densities and temperature. As electron density is increased, electron collisions become more dominant, and the effect of radiation decreases. Hence, the line ratio becomes an ineffective temperature diagnostic. The same trend occurs, to a lesser extent, for the same line ratio in iron.

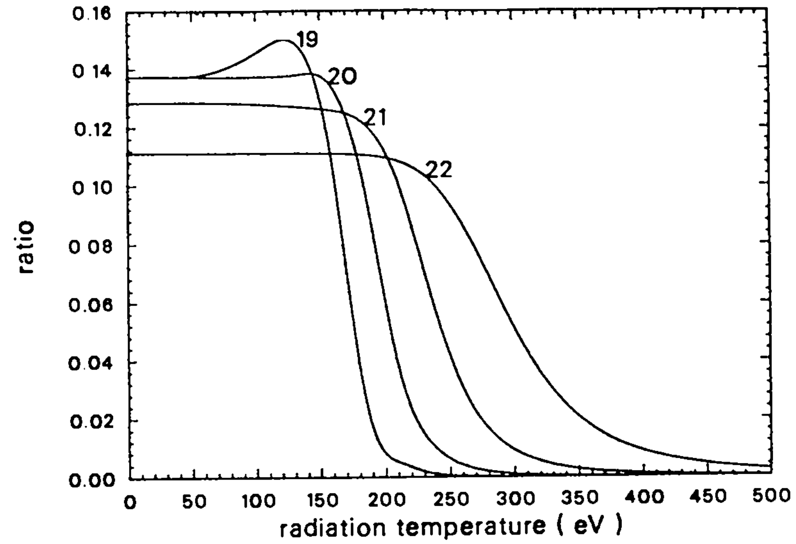

Fig. 7. The chlorine jkl/He 2-1 line ratio as a function of radiation temperature for various electron densities at $T_e = 1000$ eV. The curves are labeled by the $\log_{10} N_e$.

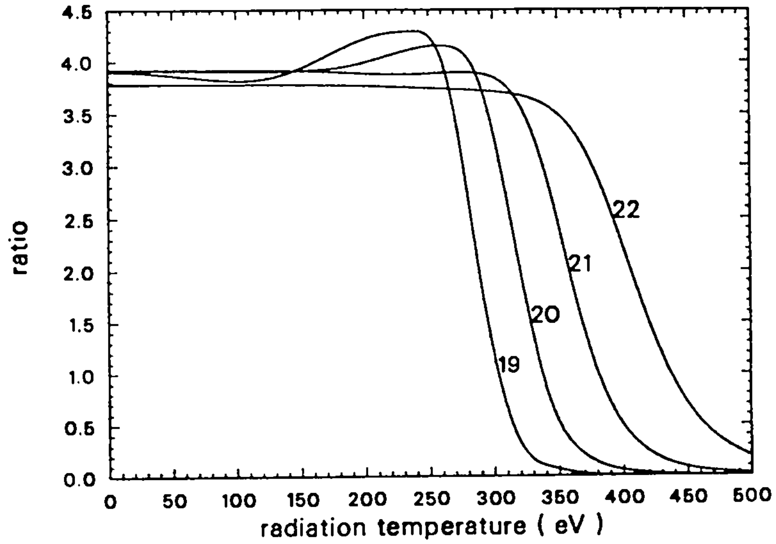

Fig. 8. The iron jkl/He 2-1 line ratio as a function of radiation temperature for various electron densities at $T_e = 1000$ eV. The curves are labeled by the $\log_{10}$ N_e.

Figures 7 and 8 show this line ratio as a function of radiation temperature at various densities for Cl and Fe, respectively. The electron temperature is fixed at $T_e = 1000$ eV. The figures predict the radiation temperatures where the $1 \rightarrow 2$ photopumping begins to have an effect on the line ratio. This occurs when the ratio begins to fall off rapidly. Note at low density, at $N_e \sim 10^{19}$, a bump occurs before the 1-2 falloff. This enhancement is probably due to $2s \rightarrow 2p$ photoexcitations. The

$$\frac{2p^2\,{}^1D_2 \rightarrow 1s2p\,{}^1P_1}{2p\,{}^2P \rightarrow 1sp^2S}$$

(He sat/H 2-1) line ratio[13] for Cl and Fe was also studied. The $T_r = 0$ result is a strong function of temperature, and the variation of the line ratio with

T_r is similar to the *jkl*/He 2-1 ratio discussed above. The 1*s* → 2*p* photoexcitation causes the line ratio to decrease for $T_r \geq 200$ eV in Cl. For Fe, the line ratio is rather insensitive to radiation.

Figure 9 shows the

$$\frac{1s2p\ {}^1P_1 - 1s^2\ {}^1S_0}{2p\ {}^2P - 1s\ {}^2S} \qquad (8)$$

(He 2-1 / H 2-1) line ratio for Cl as a function of electron temperature at Ne = 10^{19} cm^{-3}. This ratio is a strong function of temperature because it depends mostly on the relative amounts of He-like ions to H-like ions through the ionization balance. The $T_r = 0$ and $T_r = 100$ results are similar because the ionization balance is essentially unchanged by the radiation field. As T_r is increased, the ionization balance is affected and these differences become apparent in the line ratio. The result for iron (not shown) shows very little sensitivity (~20%) to radiation, even at $T_r = 300$ eV. The ratio has values greater than 100 below about $T_e = 2000$ eV due to the pre-dominance of He-like ions (see Fig. 1e).

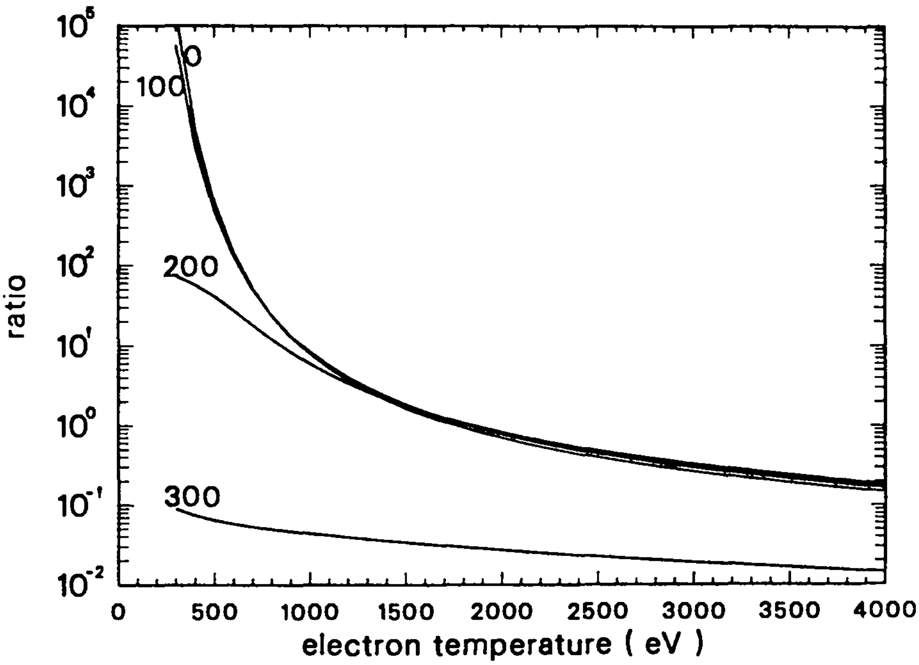

Fig. 9. The chlorine He 2-1/H 2-1 line ratio as a function of electron temperature for various values of radiation temperature at $T_e = 10^{19}$ cm^{-3}. The curves are labeled by radiation temperature in eV.

The result for the line ratio involving the $n = 3$ upper level in the numerator and denominator of Eq. (8) is nearly identical to the $n = 2$ result since ionization balance is the determining factor. It is sometimes advantageous to use the $n = 3$ line ratios as a diagnostic because of smaller optical depth effects.

C. Electron Density Sensitive Line Ratios

Figure 10 shows the

$$\frac{1s2p\ {}^3P_1 - 1s^2\ {}^1S_0}{1s2p\ {}^1P_1 - 1s^2\ {}^1S_0}$$

(IC/He 2-1) line ratio for He-like Cl as a function of electron density at $T_e = 1000$ eV. The transition in the numerator is often referred to as the intercombination (IC) line. The ratio is normally considered to be density sensitive for $T_r = 0$. Since the oscillator strength from the $1s2p\ {}^3P_1$ to the ground level is small (the transition is spin forbidden), population builds up in the ${}^3P$ multiplet through electron collisions. As the electron density is increased, further electron collisions depopulate the ${}^3P$, causing the line ratio to fall. The $T_r = 0$ curve in Fig. 10 shows this behavior and the $T_r = 100$ eV shows little difference. However, for $T_r = 200$ eV, the line ratio at low density is significantly decreased because of photoexcitations from the ground state to the ${}^1\mathrm{P}_1$ level. As electron density is increased from 10^{19}, the line ratio gets larger because a rising of ${}^3P$ state population due to electron collisions. At about $N_e = 10^{21}$ the depopulation mechanism takes hold and the line ratio decreases causing a maximum in the curve. At $T_r = 300$ eV, the line ratio is almost completely independent of electron density. Note that all curves approach the same limit as N_e get large where collision processes dominate.

Fig. 10. The chlorine He IC/H 2-1 line ratio as a function of electron density for various of radiation temperatures at T_e = 10^{19} cm^{-3}. The curves are labeled by radiation temperature in eV.

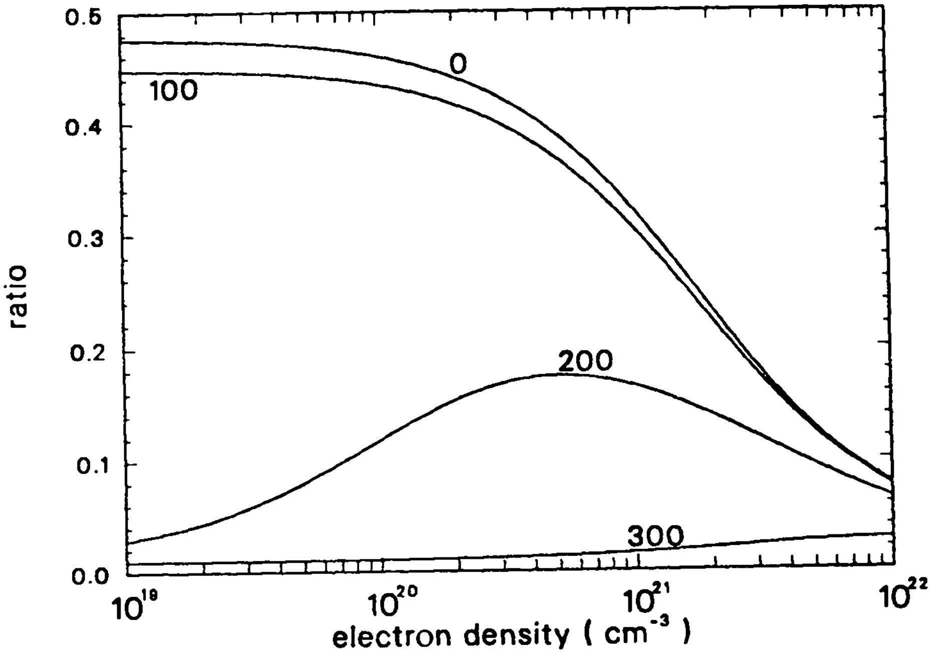

Fig. 11. The iron He IC/H 2-1 line ratio as a function of electron density for various radiation temperatures at T_e = 10^{19} cm^{-3}. The curves are labeled by radiation temperature in eV.

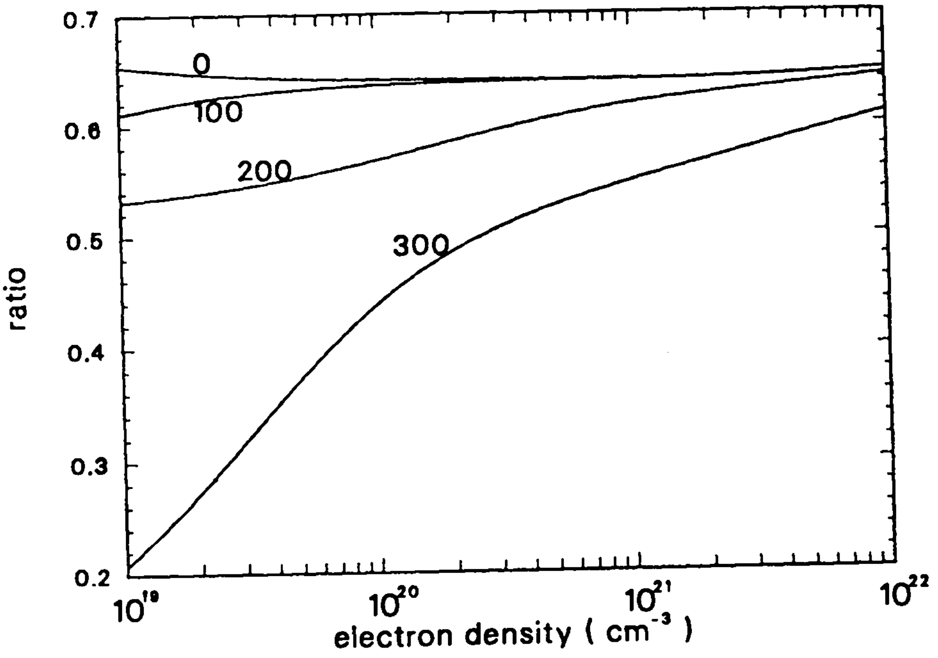

Figure 11 considers the intercombination line ratio for iron. The $T_r = 0$ result indicates that intercombination line ratio is not sensitive to electron density in this range. Unlike Cl, the oscillator strength for the ${}^3P_1$ transition to the ground state increased by a factor of 10 due to the larger spin-orbit interaction. The more rapid spontaneous decay to the ground state negates the low density populating mechanism discussed above for chlorine. It also shows that line ratios do not necessarily obey simple scaling rules from one nuclear charge to another. The $T_r > 0$ results deviate from the $T_r = 0$ case according to the amount of photoexcitation from the ground level to the preferred ${}^1P_1$ level. The largest difference is about a factor of 3 for $T_r = 300$ and low density. The curves approach eachother at lower electron densities than for chlorine. Note that the intercombination line of iron is much less sensitive to 200 eV radiation than chlorine.

The ratios of certain satellite lines of Li-like and He-like ions have been used to determine electron density.[4] Usually, the upper level of one line is mainly populated by collisional excitation, and the other is fed by dielectronic capture, making the ratio sensitive to electron density. However, these ratios were found to have a small variation (less than a factor of 2) in the density range studied here, even in the presence of radiation. These ratios become better diagnostics at electron densities higher than those considered here.

V. Conclusions

An externally applied black body radiation field with temperatures of a few hundred electron volts can have a significant effect on the spectroscopic properties of low to mid-Z plasmas in the electron temperature and density range considered here. In general, the effect is greater for Cl than Fe at a given radiation temperature, because the greater energy level separations in Fe. A 300-eV radiation field can fully strip Cl of all bound electrons, while Fe is stripped only to the He-like stage. Radiation fields can have adverse effects on line ratios which are generally considered to be diagnostics of electron temperature and density in the absence of radiation. Some line ratios (such as the intercombination line ratio) are very different for Cl and Fe suggesting that simple Z-scaling arguments are not always valid.

VI. Acknowledgement

This work was done in collaboration with C. J. Keane, T. D. Shepard, and L. J. Suter, Lawrence Livermore National Laboratory.

Amplified Spontaneous Emission Produced by Large KrF Amplifiers

For further information
on this subject contact:

W. T. Leland

Los Alamos
National Laboratory
Los Alamos, NM 87545

I. Introduction

The excited KrF* molecules in large KrF amplifiers spontaneously emit photons uniformly in all directions. The photons exhibit a distribution in frequency that depends on the mixture of rovibration states of the KrF* molecules and details of the electronic transition. While escaping from the amplifier medium, the spontaneously emitted photons interact with other molecules in the media which may absorb them or in the case of KrF* molecules, enhance their numbers by induced photon emission. The totality of photons involved is referred to as amplified spontaneous emission (ASE). The amount of ASE exiting the amplifier media is the subject of this note. Since induced emission and absorbtion cross sections depend on photon frequency, the frequency distribution of the spontaneously emitted photons must be considered. The formulation in Section II deals first with the case where a single rovibration level is involved. The generalization to cases with several rovibrational states is then considered. Appropriate values for some parameters are discussed in Section III. In Section IV calculations and experimental results are considered.

II. Calculation of External ASE

The characterization of external ASE that will be used herein is its radiance which is a scalar function of position and direction; its units are photons per second per steradian per unit area normal to the direction considered. For propagation of photons in media devoid of absorbtion or gain, radiance in the direction of propagation is invariant along the propagation path. For active media radiance is modified by the amount of gain or loss experienced along the propagation path. For a non-monoenergetic group of photons it is appropriate to consider spectral radiance which is defined as radiance per unit frequency interval. Radiance is thus the integral of spectral radiance over the appropriate frequency range.

Calculation of ASE radiance at a given point and direction on the boundary of an extended media can be achieved by summing contributions resulting from spontaneous emission in each portion of the medium. Assuming straight line propagation of photons in the medium, it is clear that contributions to the selected radiance direction can arise only from those portions lying along a line in the given direction and passing through the chosen point. The geometry of the problem is illustrated in Fig. 1.

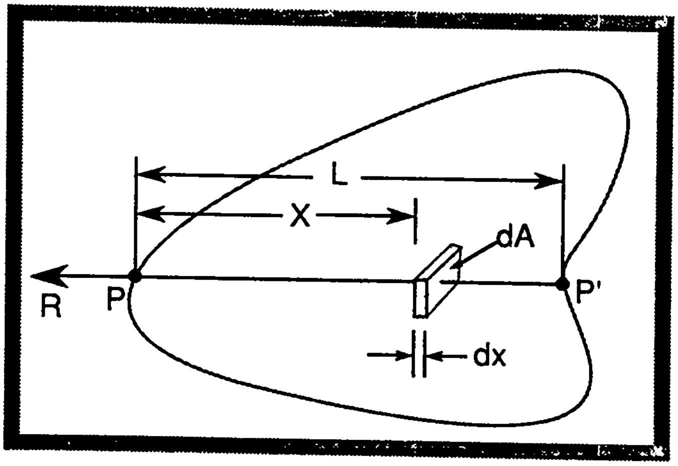

Fig. 1. Geometry for calculating ASE radiance at point P in direction R. Contributions arise from medium located along line from P to P'.

The spectral radiance $\delta R_\nu(x)$ arising from an elemental volume of area dA and length dx is given by the relation

$$\delta R_\nu(x) = \frac{n(x)\, f(\nu-\nu_0)\, dx\, dA}{4\pi\, \tau_{sp}\, dA} \quad \text{where} \qquad (1)$$

n(x) is the density of KrF* molecules at x, τ_{sp} is the spontaneous life time, and $f(\nu-\nu_0)$ a normalized frequency distribution function for the emitted photons. We have:

$$\int_{-\infty}^{\infty} f(\nu-\nu_0)\, d\nu = 1 \ . \qquad (2)$$

In its passage from point x to point P on the boundary this incremental radiance will be altered by media gain and attenuation.
We have:

$$dR_\nu(P, x) = \delta R_\nu(x) \exp\left\{\int_0^x [g(\nu-\nu_0, s) - \alpha(s)]\, ds\right\} \qquad (3)$$

where $g(\nu-\nu_0, s)$ is the frequency dependent gain coefficient at point s and α is the attenuation coefficient at point s.

The attenuation coefficient may exhibit a frequency dependence but for the calculations herein considered it will be taken as frequency independent. To obtain $R_\nu(P)$ we must sum contributions from all dx intervals from P to P'. To get R(P) we must further sum (integrate) over frequency.

For cases where the range of frequencies involved is small relative to "line center" frequency, the frequency dependence of g is to good approximation identical to the function $f(\nu-\nu_o)$. We have:

$$g(\nu-\nu_o) = g(o)\frac{f(\nu-\nu_o)}{f(o)} \; . \tag{4}$$

The inversion density n is also expressable in terms of the stimulated emission cross section and gain coefficient. We have:

$$g(\nu-\nu_o, x) = n(x)\sigma(\nu-\nu_o) \; . \tag{5}$$

The frequency ν_o can in principle be selected arbitrarily. In the development that follows it will be chosen as the "line center" frequency. This choice leads to more convenient expressions for $f(\nu-\nu_o)$.

Combining (1), (3), (4), and (5) and defining

$R_o = \dfrac{1}{4\pi\sigma(o)\,\tau_{sp}}$ we have:

$$dR_\nu(P,x) = R_o\, g(o,x)\, dx\; f(\nu-\nu_o) \exp\left\{\int_o^x \left[\frac{g(o,s)\, f(\nu-\nu_o)}{f(o)} - \alpha(s)\right] ds\right\} \tag{6}$$

$$= R_o\, f(o) dx \left\{\frac{\dfrac{f(\nu-\nu_o)}{f(o)}}{\dfrac{f(\nu-\nu_o)}{f(o)} - \dfrac{\alpha(x)}{g(o,x)}} \frac{d}{dx} \exp \int_o^x \left[\frac{g(o,s)\, f(\nu-\nu_o)}{f(o)} - \alpha(s)\right] ds\right\} \; . \tag{6a}$$

From (6a) an integration by parts yields

$$R_\nu(P) = \int_o^L dR_\nu(P,x) = R_o\, f(o)\left\{\exp\left(\bar{g}(o)L\, \frac{f(\nu-\nu_o)}{f(o)} - \bar{\alpha}L\right) h(L) - h(o)\right\}$$

$$-\int_{o}^{L} dx \left(\frac{dh}{dx}\right) \exp\left[L\bar{g}(o)\,\frac{f(\nu-\nu_o)}{f(o)} - \bar{\alpha}L\right] \qquad (7)$$

where we have defined

$$h(\nu-\nu_o,x) = \frac{\dfrac{f(\nu-\nu_o)}{f(o)}}{\dfrac{f(\nu-\nu_o)}{f(o)} - \dfrac{\alpha(x)}{g(o,x)}} \quad , \qquad (8)$$

$$\bar{g}(o) = \frac{1}{L}\int_{o}^{L} g(o,x)\,dx \quad , \qquad (9)$$

$$\bar{\alpha}(o) = \frac{1}{L}\int_{o}^{L} \alpha(x)\,dx \qquad (10)$$

In obtaining (7) it has been assumed that $f(\nu-\nu_o)$ is independent of x. This is certainly reasonable for a single rovibration line in KrF which is homogeneously broadened and the broadening is relatively independent of collision interactions. For multiple rovibration lines, however, their relative abundance may vary spatially and introduce some variation in $f(\nu-\nu_o)$.

The function h depends on x principally through the ratio $\alpha(x)/g(o,x)$. If alpha is zero or if the ratio of α to g is constant there is no x dependence. One then has:

$$R_\nu(P) = R_o f(o)\,\frac{\dfrac{f(\nu-\nu_o)}{f(o)}}{\dfrac{f(\nu-\nu_o)}{f(o)} - \dfrac{\alpha}{g}}\left[\exp\left\{L\bar{g}(o)\left(\frac{f(\nu-\nu_o)}{f(o)} - \frac{\alpha}{g(o)}\right)\right\} - 1\right] \quad . \qquad (7a)$$

There are two results of interest that follow immediately from (7a).

First: $R_\nu(P)$ and consequently $R(P)$ depends only on the average gain and absorbtion coefficient along the path of length L from P to P'.

Second: For small $L\bar{g}(o)$ the ASE radiance is proportional to $L\bar{g}(o)$ and independent of the nature of $f(\nu-\nu_o)$. Expansion of the exponent in a power series in $L\bar{g}(o)\left[\frac{f(\nu-\nu_o)}{f(o)} - \frac{\alpha}{\bar{g}(o)}\right]$ yields the result for small $\bar{g}(o)L$. We obtain:

$$R_\nu(P) \equiv R_o\, f(\nu-\nu_o)\, L\bar{g}(o) \tag{11}$$

Integration over frequency and use of (2) gives

$$R(P) \equiv R_o\, L\bar{g}(o) \tag{12}$$

For larger values of $L\bar{g}(o)$, details of the frequency dependence factor $f(\nu-\nu_o)$ come into play. To illustrate this further, three forms of $f(\nu-\nu_o)$ are considered.

<u>Case A</u>: Square hat distribution with $\Delta\nu$ the full width of the square hat. For this case we have:

$$\begin{aligned} f(\nu-\nu_o) &= \frac{1}{\Delta\nu} \text{ for } \frac{\Delta\nu}{2} \leq \nu-\nu_o \leq \frac{\Delta\nu}{2} \\ &= o \text{ for all other values of } \nu-\nu_o\ . \end{aligned} \tag{13}$$

<u>Case B</u>: Lorentzian distribution with $\Delta\nu$ the full width at half maximum. In this case:

$$f(\nu-\nu_o) = \frac{2}{\Delta\nu\pi\left[\left(\frac{\nu-\nu_o}{\Delta\nu/2}\right)^2 + 1\right]} \tag{14}$$

Case C: Gaussian distribution with Δν the full width at half maximum. In this case:

$$f(\nu-\nu_o) = \frac{2}{\Delta\nu}\sqrt{\frac{\ln 2}{\pi}}\exp\left[-\ln 2\left(\frac{\nu-\nu_o}{\Delta\nu/2}\right)^2\right] . \qquad (15)$$

Integration of $R_\nu(P)$ over frequency is straightforward in Case A. We obtain

$$R_{SH}(P) = \frac{R_o \exp\{L\bar{g}(o)(1-\alpha/g)-1\}}{1-\alpha/g} . \qquad (16)$$

To perform the integration over frequency for Cases B and C we first expand the exponential function of (7a) in a power series. We obtain

$$R_\nu(P) = R_o\, f(o)\,\frac{f(\nu-\nu_o)}{f(o)}\sum_{n=1}^{\infty}\frac{(L\bar{g}(o))^n}{n!}\left[\frac{f(\nu-\nu_o)}{f(o)}-\frac{\alpha}{g}\right]^{n-1}$$

$$(7b)$$

$$= R_o\, f(o)\sum_{n=1}^{\infty}\frac{(L\bar{g}(o))^n}{n!}\,\frac{f(\nu-\nu_o)}{f(o)}\sum_{k=o}^{n-1}\left(-\frac{\alpha}{g}\right)^k\left(\frac{f(\nu-\nu_o)}{f(o)}\right)^{n-1-k}\binom{n-1}{k}$$

where $\binom{n-1}{k} = \frac{(n-1)!}{k!\,(n-k-1)!}$.

Defining

$$b_i = f(o)\int_{-\infty}^{\infty}\left[\frac{f(\nu-\nu_o)}{f(o)}\right]^i d\nu , \qquad (17)$$

$$C_{n,i} = \left(\frac{-\alpha}{g}\right)^i\binom{n-1}{i} , \qquad (18)$$

and

$$S_n = \sum_{k=o}^{n-1} C_{n,k}\, b_{n-k} \qquad (19)$$

we obtain

$$R(P) = \int_{-\infty}^{\infty} R_\nu(P)\, d\nu = R_o \sum_{n=1}^{\infty} \frac{L\bar{g}(o)^n}{n!} S_n \ . \qquad (20)$$

To evaluate the b coefficients of (17) it is convenient to make the substitutions

$$y = \frac{\nu - \nu_o}{\Delta\nu/2} \qquad (21)$$

and

$$d\nu = \frac{\Delta\nu}{2}\, dy \ . \qquad (22)$$

For the Lorentzian Case B we then have

$$b_i = \frac{2}{\pi\Delta\nu} \int_{-\infty}^{\infty} \frac{\Delta\nu}{2}\, dy \left(\frac{1}{1+y^2}\right)^i$$

$$= \frac{2}{\pi} \int_{o}^{\infty} dy \left(\frac{1}{1+y^2}\right)^i$$

or

$$b_i = 1 \text{ for } i=1$$

$$b_i = \left(\frac{2i-3}{2i-2}\right)\left(\frac{2i-5}{2i-4}\right) \cdots \left(\frac{1}{2}\right) \text{ for } i \geq 2 \qquad (23)$$

When α/g is zero S_n is equal to b_n as can be seen from examination of (7b). Using (20) we can then write for this special case:

$$R_L(P) = R_o \sum_{n=1}^{\infty} \frac{(L\bar{g}(o))^n b_n}{n!}$$

$$= R_o \sum_{n=1}^{\infty} (L\bar{g}(o))\, a_n \qquad (24)$$

where $a_1 = 1$ and $\frac{a_{k+1}}{a_k} = \frac{2k-1}{2k(k+1)}$

For a Gaussian line shape using (15), (21), and (22) we obtain

$$b_i = \frac{2}{\Delta\nu} \sqrt{\frac{\ln 2}{\pi}} \int_{-\infty}^{\infty} \frac{\Delta\nu}{2}\, dy \left[\exp\left(-y^2 \ln 2\right)\right]^i$$

$$= 2\sqrt{\frac{\ln 2}{\pi}} \int_{0}^{\infty} dy \exp\left(-iy^2 \ln 2\right) \ . \qquad (25)$$

Letting $z = y\sqrt{i \ln 2}$, (25) becomes

$$b_i = \frac{2}{\sqrt{i\pi}} \int_{0}^{\infty} dz \exp^{-z^2}$$

$$= \frac{1}{\sqrt{i}} \ . \qquad (26)$$

When α/g is zero, we obtain the formula:

$$R_G(P) = R_o \sum_{n=1}^{\infty} \frac{(L\bar{g}o)^n b_n}{n!}$$

$$= R_o \sum_{n=1}^{\infty} (L\bar{g}(o))^n d_n \qquad (27)$$

where $d_1 = 1$ and $\frac{d_{k+1}}{d_k} = \frac{1}{(n+1)} \sqrt{\frac{n}{n+1}}$.

Note that the power series representation for both the Lorentzian and Gaussian line shape converges for all values of $L\bar{g}(o)$. Note also that the values of $R_{SH}(P)$, $R_L(P)$, and $R_G(P)$ do not depend on the parameter $\Delta\nu$ (full width at half maximum) used in defining the line shape. However, if a line were somehow broadened this would imply lower gain for a given inversion and hence less ASE.

For large values of $L\bar{g}(o)$ the power series representations converge slowly. By using a power series in $1/L\bar{g}(o)$ one can ascertain the behavior for large $L\bar{g}(o)$. The resulting (asymptotic) series do not converge for any value of $L\bar{g}(o)$ but nevertheless provide a good representation if the series is judiciously truncated and its use limited to values of $L\bar{g}(o)$ exceeding an appropriate minimum value. To arrive at the asymetric series we begin with Eq. (7a), factor out $\exp\left\{L\bar{g}(o)\left[1-\frac{\alpha}{g}\right]\right\}$ and obtain

$$R_\nu(P) = R_o f(o)\exp[L(\bar{g}(o)-\alpha)]\,\frac{\dfrac{f(\nu-\nu_o)}{f(o)}}{\dfrac{f(\nu-\nu_o)}{f(o)}-\dfrac{\alpha}{g}}\left\{\exp\left[L\bar{g}(o)\left(\frac{f(\nu-\nu_o)}{f(o)}-1\right)\right]-\exp[-L\bar{g}(o)-\alpha]\right\}. \qquad (7c)$$

Upon the further substitution

$z = f(o)\,(\nu-\nu_o)$

and integration over frequency we obtain for the Lorentzian line shape:

$$R_L(P) = R_o\exp[L\bar{g}(o)-\alpha]\int_{-\infty}^{\infty}dz\,\frac{\dfrac{1}{1+\pi^2z^2}}{\dfrac{1}{1+\pi^2z^2}-\dfrac{\alpha}{g}}\left\{\exp\left(\frac{-\pi^2z^2L\bar{g}(o)}{1+\pi^2z^2}\right)-\exp[-L(\bar{g}(o)-\alpha)]\right\}. \qquad (28)$$

The further substitution

$$x = \sqrt{L\bar{g}(o)}\, z\pi$$

gives:

$$R_L(P) = R_o \frac{\exp[L(\bar{g}(o)-\alpha)]}{\pi \sqrt{L\bar{g}(o)}} \int_{-\infty}^{\infty} dx \frac{\frac{1}{1+\lambda x^2}}{\frac{1}{1+\lambda x^2} - \frac{\alpha}{g}} \left\{ \exp\left[\frac{-x^2}{1+\lambda x^2}\right] - \exp\left[\frac{-\left(1-\frac{\alpha}{g}\right)}{\lambda}\right] \right\} \tag{29}$$

where the parameter λ equals $1/L\bar{g}(o)$. Expansion of the integrand in a power series in λ provides the required asymptotic series. The term $\exp\left[\frac{-(1-\alpha/g)}{\lambda}\right]$ yields the null series in λ. The leading term yields the behavior for large Lg(o). We have for $L\bar{g}(o) >>1$ in the Lorentzian case

$$R_L(P) \equiv R_o \frac{\exp[L(\bar{g}(o)-\alpha)]}{\sqrt{L\bar{g}(o)}\left(1-\frac{\alpha}{g}\right)} \frac{2}{\pi} \int_o^{\infty} dx \exp^{(-x^2)}$$

$$= R_o \frac{\exp[L(\bar{g}(o)-\alpha)]}{\sqrt{\pi}\sqrt{L\bar{g}(o)}\left(1-\frac{\alpha}{g}\right)} \tag{30}$$

For the Gaussian line shape, we obtain for the equivalent of (28):

$$R_G(P) = R_o \exp[L(\bar{g}(o) -\alpha)] \int_{-\infty}^{\infty} dy \frac{\exp\left[-\frac{\pi z^2}{Lg(o)}\right]}{\exp\left[\frac{-\pi z^2}{L\bar{g}(o)}\right] \frac{-\alpha}{g}}$$

$$\left\langle \exp\left\{L\bar{g}(o) \exp\left[\frac{\pi z^2}{L\bar{g}(o)} -1\right]\right\} -\exp[L(\bar{g}(o)-\alpha)] \right\rangle . \tag{31}$$

The further substitution

$$x = \sqrt{L\bar{g}(o)}\, \sqrt{\pi}\, z$$

gives:

$$R_G(P) = R_o \frac{\exp[L(\bar{g}(o)-\alpha)]}{\sqrt{\pi}\,\sqrt{L\bar{g}(o)}} \int_{-\infty}^{\infty} dx \, \frac{\exp\left[-\lambda x^2\right]}{\exp\left[-\lambda x^2\right] - \frac{\alpha}{g}} \left\{ \exp\left[\frac{1}{\lambda}\left(\exp\left[-\lambda x^2\right]-1\right)\right] - \exp\left[-\frac{1-\alpha/g}{\lambda}\right] \right\} . \tag{32}$$

Noting that

$$\exp\left[-\lambda x^2\right] - 1 = -\lambda x^2 + \lambda^2 x^4 + \ldots \quad .$$

The leading term in the λ expansion yields

$$R_G(P) = R_o \frac{\exp[L(\bar{g}(o) - \alpha)]}{\sqrt{L\bar{g}(o)}\,(1-\alpha/g)} \frac{2}{\sqrt{\pi}} \int_o^{\infty} dx \; e^{-x^2}$$

$$= R_o \frac{\exp[L(\bar{g}(o) - \alpha)]}{\sqrt{L\bar{g}(o)}\,(1-\alpha/g)} \tag{33}$$

If one invokes the Einstein equilibrium theory relating the A and B coefficients one obtains the relation

$$\sigma(o)\,\tau_{sp} = \frac{\lambda_o^2 \eta \; f(o)}{8\pi} \tag{34}$$

where η is the refractive index of the medium. The quantity R_o then can be expressed as:

$$R_o = \frac{2}{\lambda_o^2 \eta \; f(o)} . \tag{35}$$

As noted earlier, the symbol zero does not necessarily imply line center. f(o), λ_o, and R_o all relate to a selected wavelength and the function f(ν-ν_o) is to be constructed accordingly. The assumptions of identical frequency dependencies for gain and spontaneous emission is equivalent to neglecting the variation of ν in the range of interest.

Quantum mechanical non equilibrium theories yield similar results for regimes of time and ASE intensities of interest.[a]

When several excited states emit spontaneously into the frequency range of concern, one can generalize Eq. (1) by summing the contribution from each state. We have

$$\delta R_\nu(x) = \sum_i \frac{n_i(x)\ f_i(\nu-\nu_o)}{4\pi\ \ \tau_{i,sp}}\, dx \tag{36}$$

where $n_i(x)$ is the population density of state i, $\tau_{i,sp}$ is the spontaneous life time of state i, and $f_i(\nu-\nu_o)$ is the normalized frequency distribution function for state i.

The states are presumed distinct and emit independently. For propagation through an active medium, however, all states contribute to the amplification of photon flux originating from different states. The overall gain from the various states is given by

$$g_c(\nu-\nu_o,x) = \sum_i \left[n_i(x)\ \sigma_i(o)\ \frac{f_i(\nu-\nu_o)}{f_i(o)} \right] \tag{37}$$

$$= \sum_i g_i(o,x)\ \frac{f_i(\nu-\nu_o)}{f_i(o)}\ . \tag{37a}$$

The relation corresponding to (6) is:

$$\frac{dR_\nu(P,x)}{dx} = \sum_i \frac{n_i(x)\ f_i(\nu-\nu_o)}{4\pi\,\tau_i}\ \exp \int_o^x [g_c(\nu-\nu_o,x) - \alpha]\ ds\ . \tag{38}$$

---

[a] See for example, "The Quantum Theory of Light ", Chapter 2, by Rodney Loudon, Clarendon Press Oxford 1982

Using (35) we obtain:

$$\frac{dR_\nu(P,x)}{dx} = \frac{2}{\lambda_o^2\eta}\, g_c(\nu-\nu_o,x)\, \exp\int_o^x [g_c(\nu-\nu_o,x) - \alpha]\, ds \quad .(38a)$$

as before an integration by parts and the assumption of no x dependence of ratio of α to $g_c(\nu-\nu_o)$ yields the counterpart to (7a)

$$R_\nu(P) = \left(\frac{2}{\lambda_o^2\eta}\right) \frac{1}{1 - \dfrac{\alpha(x)}{g_c(\nu-\nu_o,x)}} [\exp(L\bar{g}_c(\nu-\nu_o) - \alpha L) - 1] \ . \qquad (39)$$

For small $L(g_c-\alpha)$

$$R_\nu(P) \equiv \frac{2}{\lambda_o^2\eta} L\bar{g}_c(\nu-\nu_o) = \frac{2L}{\lambda_o^2\eta} \sum_i \bar{n}_i(x)\, \sigma_i(o) \frac{f_i(\nu-\nu_o)}{f_i(o)} \ . \qquad (40)$$

Integration over frequency gives

$$R(P) \equiv \frac{2}{\lambda_o^2\eta} L \sum_i \frac{\bar{n}_i(x)\, \sigma_i(o)}{f_i(o)} \qquad (41)$$

$$= \frac{L}{4\pi} \sum_i \frac{\bar{n}_i(x)}{\tau_i} = \frac{LN}{4\pi\bar{\tau}} = \frac{L\, g_c(o)}{4\pi\bar{\tau}\, \bar{\sigma}_c(o)} \qquad (42)$$

where

$$N = \sum_i \bar{n}_i(x) \ , \qquad (43)$$

$$\frac{1}{\tau} = \frac{1}{N} \sum_i \bar{n}_i \left(\frac{1}{\tau_i}\right) \ , \qquad (44)$$

and $\bar{\sigma}_c(o) = \dfrac{1}{N} \sum_i \bar{n}_i \sigma_i(o)$. (45)

For large values of g_cL, Eq. (39) must be integrated over frequencies. Defining

$$g_c(\nu-\nu_o) = g_c(o)\,\frac{f_c(\nu-\nu_o)}{f_c(o)} \tag{46}$$

where

$$g_c(o) = \Sigma\, n_i\sigma_i(o) = N\sigma(o)\ , \tag{47}$$

$$f_c(o) = \frac{\lambda_o^{\,2}}{8\pi}\,\overline{\sigma}(o)\,\overline{\tau}\ , \tag{48}$$

$$f_c(\nu-\nu_o) = \sum_i \frac{n_i}{N}\,\frac{\overline{\tau}}{\tau_i}\,f_i(\nu-\nu_o)\ , \tag{49}$$

and

$$\int d\nu\ f_c(\nu-\nu_o) = 1 \tag{50}$$

allows (39) to be written in the form

$$R_\nu(P) = \frac{f_c(o)}{4\pi\overline{\sigma}(o)\overline{\tau}}\,\frac{\dfrac{f_c(\nu-\nu_o)}{f_c(o)}}{\dfrac{f_c(\nu-\nu_o)}{f_c(o)} - \dfrac{\alpha}{\overline{g}_c(o)}}$$

$$\exp\left\{L\overline{g}_c(o)\left[\frac{f_c(\nu-\nu_o)}{f_c(o)} - \frac{\alpha}{\overline{g}_c(o)}\right] -1\right\} \tag{51}$$

which is identical to (7a) with quantities f, g and $\sigma\tau$ replaced by f_c, g_c, and $\overline{\sigma}\,\overline{\tau}$. Integration of (51) over frequency requires specification of $f_c(\nu-\nu_o)$. The result will be of the form:

$$R(P) = \frac{1}{4\pi\,\overline{\sigma}_c(o)\,\overline{\tau}}\,F \tag{52}$$

where F depends on $\bar{g}_c(o)L$, α, and the form of $f_c(\nu-\nu_o)$. In the limit of small $\bar{g}_c(o)L$, F always reverts to $\bar{g}_c(o)L$. In general

$$F = f_c(o) \int d\nu \frac{\dfrac{f_c(\nu-\nu_o)}{f_c(o)}}{\dfrac{f_c(\nu-\nu_o)}{f_c(o) - \dfrac{\alpha}{g_c(o)}}} \quad \exp\left\{ L\, \bar{g}_c(o) \left[\frac{f_c(\nu-\nu_o)}{f_c(o)} - \frac{\alpha}{g_c(o)} \right] -1 \right\} . \tag{53}$$

III. The value of $\bar{\sigma}_c(o)\bar{\tau}$

To proceed with the calculation of external ASE via Eq. 53, a value for $\bar{\sigma}_c(o)\bar{\tau}$ must be assigned. It is evident from their definitions (Eq. 44 and 45) that the appropriate value for both $\bar{\sigma}_c(o)$ and $\bar{\tau}$ will depend on the mixture of rovibrational states involved. The mixture that obtains in a given case will depend on kinetic details involved in the formation of KrF* and its subsequent interactions with other molecules in the media. Tiee et al[1] found substantial variation in the spectra of KrF* produced by photolysis of KrF_2 with radiation of different wave lengths. For the relatively low pressures and short times involved in their experiment the measured distribution would be sensitive to the mix of rovibrational states formed in the photoexcitation reaction. Tamagake and Setser[2] found similar variation when KrF* is formed by interaction of metastable Kr with F_2, NF_3, and CF_3OF. Pummer et al[3] observed the time evolution of rovibrational states by observing the time evolution of emitted radiation at different wave lengths. Thus the appropriate value of $\bar{\sigma}_c(o)\bar{\tau}$ is clearly not a universal quantity. In many cases, however, the externally observed emissions from KrF* will be dominated by a semi-steady-state distribution of rovibrational states with a predominance of the low vibration states. Theoretical calculations predict the values of $\sigma(o)$ and τ do not vary drastically for the first three or four vibration levels.[12] The proportion of molecules in higher vibrational levels (20 or 30%) will not be a serious problem. This circumstance arises because the higher vibration levels contribute little to the overall gain in the frequency region where the bulk of spontaneously emitted photons are produced.

There are several ways in which the product $\bar{\sigma}_c(o)\,\bar{\tau}$ can be obtained experimentally. In principle at least, a measurement of the emission spectra from a "thin" source will provide the answer via the formula

$$\bar{\tau}\,\bar{\sigma}_c(o) = \frac{s(o)}{\int s(\nu-\nu_o)d\nu}\left[\frac{8\pi}{\lambda_o^{2}}\right] \qquad (54)$$

where $s(\nu-\nu_o)$ is the measured signal in units proportional to photons cm^{-2} sec^{-1} per unit frequency interval and the integral extends over the range of concern. This approach does not appear to have been used directly but rather in conjunction with reduction of data via application of theoretical models. By adjusting the mixture of states and details of potential curves a "best fit" of the theoretical model to spectral data is effected. The theoretical model using adjusted quantities is then used to calculate quantities such as $\bar{\sigma}_c(o)\,\bar{\tau}$. Tellingheusin et al[4] fitted their observed spectra with a "thermalized" 360°K distribution of states and report a $\sigma\tau$ value of $1.7\pm.2\times10^{-24}$ cm^2 sec. This value is frequently quoted in the literature. It should be noted, however, that Tellingheusin's fit to the experimental data was not very good. Patterson and Hanson[5] have analysed spectral data from Murray and Powell[6] as well as the data from Tellingheusin. They used potential curves produced via ab initio calculation by Hay and Dunning.[7] By adjusting the mixture of states they report a good fit to the data of Murray and Powell. The best fit state distribution was far from a thermalized one and gave a peak $\sigma\tau$ value of $1.2\text{x}10^{-24}$ cm^2 sec. A 300°K thermalized distribution applied to the Tellingheusin data gave a $\sigma\tau$ of $1.8\text{x}10^{-24}$ cm^2 sec.

The Tellingheusin and Murray spectra were produced by e-beam excitation in gas mixtures at "high" pressures. They do not state the gL product of the media which they measured the spectra for and it is not possible to judge whether the spectra qualify as due to a "thin source". To qualify for "thin" would require a negligible second term in the power series expansion of (51). The two term expansion of (51) for $R_\nu(P)$ gives:

$$R_\nu(P) = \frac{g_c(o)L}{4\pi\,\bar{\sigma}_c(o)\,\bar{\bar{\tau}}}\left\{f_c(\nu-\nu_o) + \frac{g_c(o)L}{2}\,f_c(\nu-\nu_o)\left[\frac{f_c(\nu-\nu_o)}{f_c(o)} - \frac{\alpha}{g_c(o)}\right]\right\} \; . \tag{55}$$

For a negligibly altered spectra one would like:

$$\frac{g_c(o)L}{2}\left[\frac{f_c(\nu-\nu_o)}{f_c(o)} - \frac{\alpha}{g_c(o)}\right] << 1 \; . \tag{56}$$

Distortion of the spectra at $\nu=\nu_o$ occurs unless

$$\frac{g_c(o)L}{2}\left(1 - \frac{\alpha}{g_c(o)}\right) << 1 \; . \tag{57}$$

A second method for determining $\bar{\sigma}_c(o)\,\bar{\tau}$ involves simultaneous measurement of $g_c(o)$ and R(P) for a "thin" source . Since we than have $g_c(o) = \bar{\sigma}_c(o)\,N$ and $R(P) = \frac{LN}{4\pi\,\bar{\tau}}$ one obtains:

$$\bar{\sigma}_c(o)\,\bar{\tau} = \frac{L}{4\pi}\,\frac{g_c(o)}{R(P)} \tag{58}$$

This method is straightforward but does not appear to have been used in published papers relevant to the subject.

A third method for determining $\bar{\sigma}_d(o)\bar{\tau}$ involves measuring $\bar{\tau}$ and $\bar{\sigma}_d(o)$ in separate experiments. The usual questions pertaining to the distribution of rovibrational states arises. Experimental measurements of $\bar{\tau}$ have been reported by several investigators.[1,8,9] In all experiments KrF* was produced by photolysis of KrF_2 and the time decay of spontaneous emission observed. Measurements were made at low pressure and extrapolated to zero pressures. The reported values of τ, however, range from 6.8[9] to 9.5[1] nanoseconds. Patterson and Hanson[10] have suggested that "B-C state mixing" might have influenced the measurements. McCowan[11] examined the B-C state mixing question also. At the low pressures used in the experiments it is difficult to believe there would be sufficient B-C mixing to compromise the observed decay of the B state. Some variation in the measurements may be traceable to variation in rovibrational state mixtures. Theoretical calculations[2,6] indicate a moderate dependance of life time on the vibrational state involved. Both Tamagake et al[2] and Morgan et al[12] use the Hay and Dunning[7] potential curves to calculate τ. Morgan et al report calculated values of τ from 7.0 to 8.6 nanoseconds as the vibrational quantum number ranges from 0 to 10. Dunning and Hay[13] report a calculated value of 6.7 nanoseconds, presumably for $v=0$.

Measured values of σ are obtained from short pulse energy extraction experiments for which the quantity $h\nu/\sigma$ is derived. Using pulses with duration of a few picoseconds, Szatmari and Schafer[14] report a value of 2×10^{-3} joules/cm^2 for $h\nu/\sigma$. Taylor et al[15] in a similar experiment find a value of $1.8\text{x}10^{-3}$ joules/cm^2. Bucksbaum et al[16] report a value of $2.1\text{x}10^{-3}$ joules per cm^2. For a 2 nanosecond pulse Banic et al[17] report a value of $3.2\text{x}10^{-3}$ joules/cm^2. All the measurements noted above were made in discharge type amplifier and are based on data reduction using a Frantz-Nodvik[18] formulation of output versus input. The derived value is thus model dependent. Models modified to take into account semi overlapping states, absorbtion, etc. will result in different derived values of σ. This is illustrated in Fig. 2. Predictions obtained with three different models are compared with the Frantz-Nodvik curve with E_{sat} set equal to 2 millijoules/cm^2 and a small signal gain of exp(10). In all models the small signal "net" gain was set equal to exp (10) and the value of E_{sat} adjusted to provide the same E_{in} at a net amplifier gain of 100. In case (1) a non saturable absorbtion to gain coefficient ratio α/g of .07 was used.

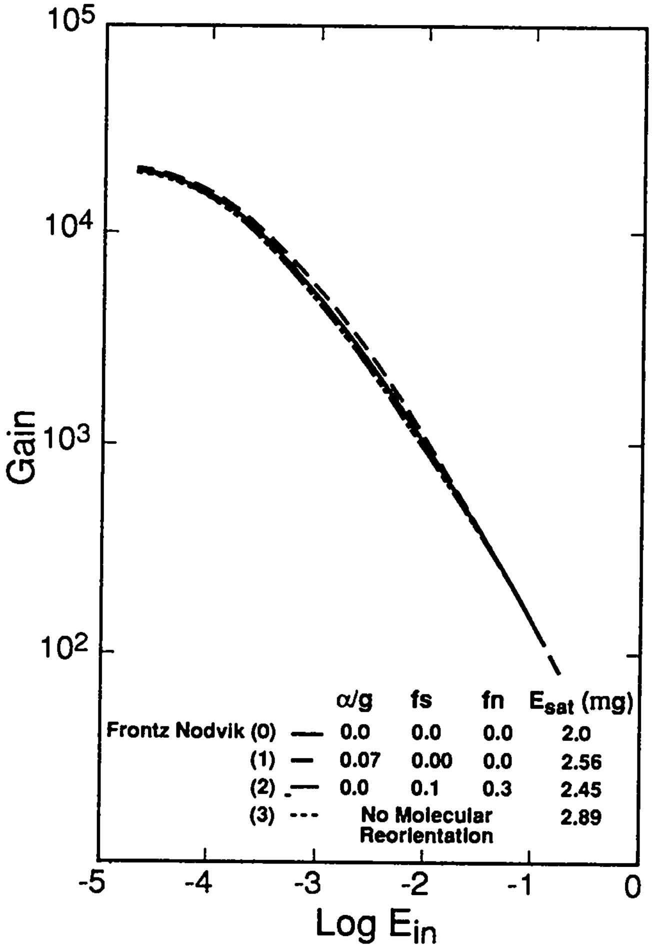

Fig. 2. Deriving E_{sat} using different models.

In Case (2), two partially overlapping states were used. The secondary state was assumed to have 30% as much population as the primary state. The cross section for the secondary state at line center of the primary state was taken as 10% the cross section of the primary state. Case (3) assumes that no molecular reorientation occurs and that the extracting beam is polarized. Szatmari and Schafer[19] observed effects they ascribe to finite molecular reorientation times. The time constant appeared to be on the order of .9 picoseconds with an amplifier pressure of 2.5 bar. The models used are based on rate equation formulations. The possibility of coherent effects must also be considered for "very short" pulses. The situation in regard to KrF amplifiers has been examined by Milonni et al.[20] They find no significant impact on the energetics of pulse extraction in KrF amplifier with pulse lengths of 1 picosecond.

Other values of $\sigma\tau$, have been noted in the literature. The group at AVCO report $(1.6\text{x}10^{-24})$[21], and $(1.75\text{x}10^{-24})$[22] for this quantity but the details of how they arrived at the value are not specified in the articles cited.

Besides the value of $\sigma\tau$, the frequency distribution of gain and spontaneously emitted photons have a bearing on the amount of external ASE produced in high gain KrF amplifiers. The frequency spectra depends on the distribution of rovibrational states. Milonni et al[20] suggest that for the v=o ground state, a nearly Gaussian shape should obtain. The spectra from states with $n \geq l$ are not Gaussian.[5] Their contribution to the shape in the vicinity of "line center" tends to broaden the line.

IV. Experimental Measurements of External ASE

External ASE has often been used as a diagnostic to monitor KrF laser media. When observing desired laser output it presents unwanted background. Numerical analysis based on formulations detailed above have been applied to several sets of experimental data. Within error limits inherent in the experimental results and parameters used, the analyses produce predictions in agreement with measured results. It is nevertheless the case that no definitive experiment has yet been performed to allow a careful assessment of how precise the predictions are.

Thomas et al[23] made a quantitative measurement of the radiance from the Lumonics Aurora front end laser. Two apertures were used to define both an area and solid angle of ASE emerging from the pumped media. Time history of the radiance was observed with a fast photodiode while the time integrated intensity was measured in a calibrated calorimeter. The measured radiance in watts/cm^2/steradian is shown in Fig. 3. Using $\sigma\tau = 1.8\text{x}10^{-24}$ cm^{2}sec and a Lorentzian line shape, the calculated gl product is also shown in Fig. 3. No direct measurement was made of small signal gain coefficient. The length of amplifier media is 90 cm which then yields a calculated maximum gain coefficient of 12.6%/cm which is reasonable.

John Oertel et al[24,25] report measurements and comparison with calculations for the Aurora large aperture module.

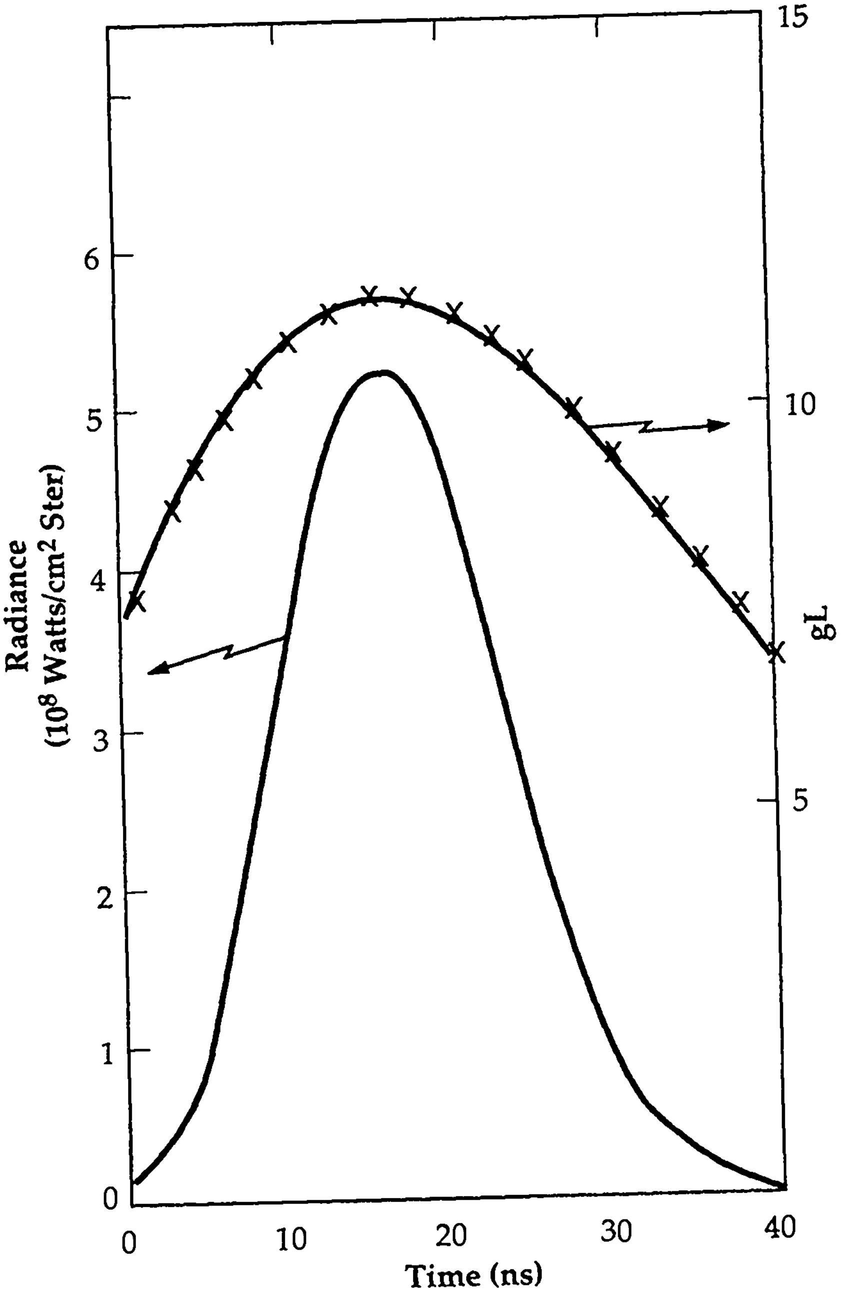

Fig. 3. Measured radiance from Lumonics ampifier and calculated gl.

In more recent measurements Czuchlewski et al[26] measured the time integrated radiance from the Aurora PA amplifier with a calorimeter and a defined geometry. PA amplifier measurements were made with and without a mirror at the far end. An analysis of the results was performed by using the measured (on an earlier experiment) time history of side light to infer a time dependence of amplifier gain.

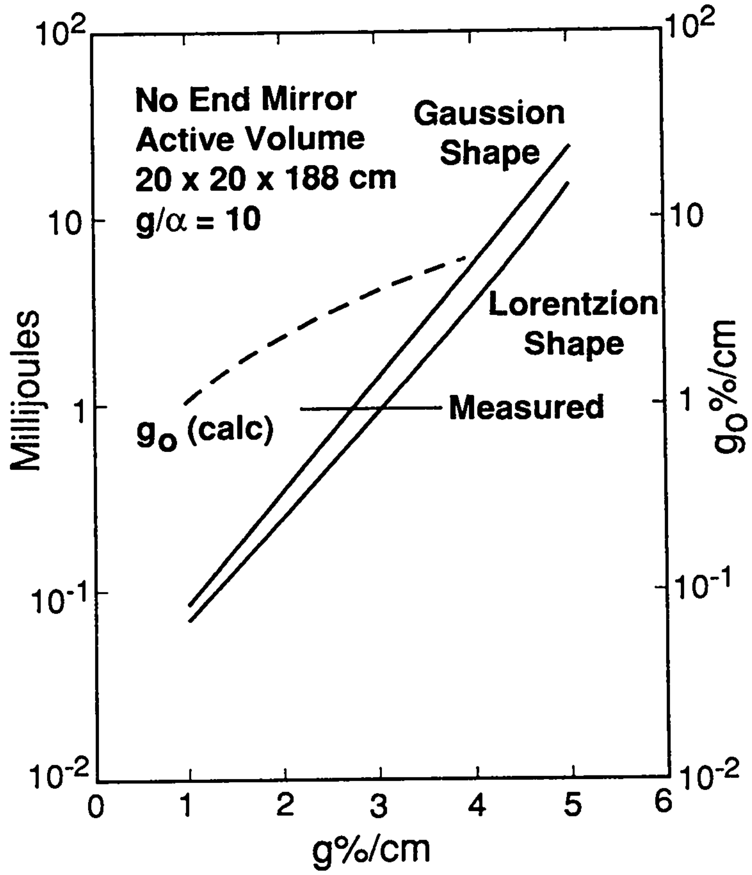

Fig. 4. Measured and calculated single pass external ASE from the PA amplifier, along with calculated g_o. The model includes optic transmission losses and losses due to absorption in the amplifier.

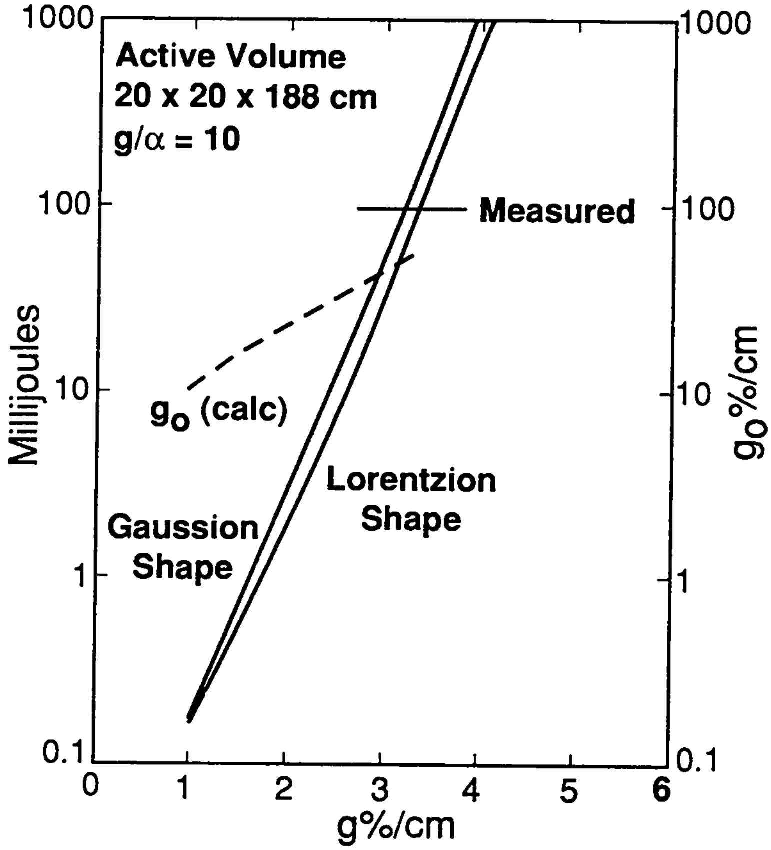

Fig. 5. Measured and calculated double pass external ASE from the PA amplifier, along with calculated g_o. The model includes optic transmission losses and losses due to absorption in the amplifier.

Fig. 4 and 5 show calculated curves of energy (time-integrated intensity times area) versus small signal gain coefficient. The two curves shown are for Lorentzian and Gaussian line shapes respectively. The measured output energy is indicated by horizontal lines. The calculations are consistent with a small signal gain coefficient of about 3.3%/cm. This is somewhat higher than values measured earlier on the same amplifier prior to making repairs. Calculated values of the gain coefficient g_0 that would obtain if no internal ASE were present are also shown.

External ASE contributes to prepulse in target shooting systems. The analysis for systems is relatively complex. It is necessary to specify time dependent details of all amplifiers involved on an individual basis as well as including their relative timing. The presence of an extracting beam and its timing must also be considered since it has major impact on system gain. In multichannel systems such as Aurora and Mercury, the manner in which system architecture affects timing in different channels must also be considered. Interamplifier and amplifier-to-target beam transport must also be taken into account. Two system studies have been made, one version of Aurora[27] and one for a downsized Aurora[28]. R. Krystal[29] measured total prepulse power for the Aurora system. The measured value was approximately 1/3 of the calculated value. The calculated value was based on "best estimate" values for amplifier performance and timing. A trivial change in assumed performance or timing could easily effect agreement with Krystal's measurements. An often specified parameter in regard to prepulse tolerance is power density. Calculated ASE power densities based on "perfect optics" generally far exceed acceptable levels. Non perfect optics will lower the average power density and most likely the peak power density as well. For average power densities the ratio of actual beam size on target to a diffraction limited area would seem to be a legitimate correction factor. Peak power densities are more difficult to address and are not likely to scale as an area ratio.

Low Threshold Virtual Cathode Formation in a Large Area Electron Beam on an KrF Laser

For further information
on this subject contact:

V. A. Thomas,

M. E. Jones

Los Alamos
National Laboratory
Los Alamos, NM 87545

I. Introduction

One possible scenario for laser fusion is to use large aperture krypton fluoride lasers.[1,2] These lasers are pumped by large area (.1 to 2 m^2) electron beams in the 250 keV to 1 MeV range.[3] KrF lasers are not storage lasers, hence the maximum peak intensity at the output of the laser is dependent on the pumping power of the electron beams. The power in the electron beam can be increased by increasing the voltage or the current, however increasing the voltage on the electron gun both increases the difficulty in the pulse power design and requires greater gas pressure for a fixed size laser aperture in order to stop the higher energy electrons. The greater pressure increases the required strength on the hibachi and gas foil structure which separates the electron beam source from the laser of a volume, while also modifying the laser kinetics. The limits for increasing the current are the difficulty in designing large low-impedance water pulse-forming lines and the effects of the self generated field in the electron beam. By the addition of a guide magnetic field to the electron gun, the current can be increased over the self pinch limit. The applied guide magnetic field is parallel to the electron flow. The self generated field adds to the applied field to result in a net angle between the accelerating electric field and the total magnetic field. The angle will be the greatest near the edge of the electron beam. The guide field cannot be made arbitrarily large due to cost constraints and the large amount of energy stored in the guide field. The applied magnetic field should be the minimum required to provide acceptable losses near the edges of the beam when the electrons strike the hibachi due to the angle of attack determined by the total magnetic field.[4]

Recent research at NRL and simulations performed at Los Alamos indicate additional concerns when trying to reduce or eliminate the guiding magnetic field. The stability of the electron beam as it is accelerated and drifts through the hibachi to enter the gas is important. Strong oscillations will spread the electron energy distribution largely to lower energies reducing the delivered energy to the gas, increasing the foil losses, and making it more difficult to get a smooth energy deposition in lasers which are pumped from two sides. A strong instability was observed in a laser at NRL when the guide magnetic field was reduced below a critical value. In order to examine this result, the experimental arrangement and the experimental results will be described first. The simulation results will follow to confirm the basis for the physical explanation.

II. The Experiment

Figure 1 shows the design of one of the electron guns on the NIKE 20 cm driver amplifier. The electron beam is created by a cold cathode discharge which uses a 20 cm by 80 cm velveteen emitter with a parabolic curvature near the edges to prevent the halo effect. The anode is a 85% optically transmissive stainless steel screen 2.8 cm away from the velveteen. Directly behind the anode screen is the hibachi structure. The hibachi is

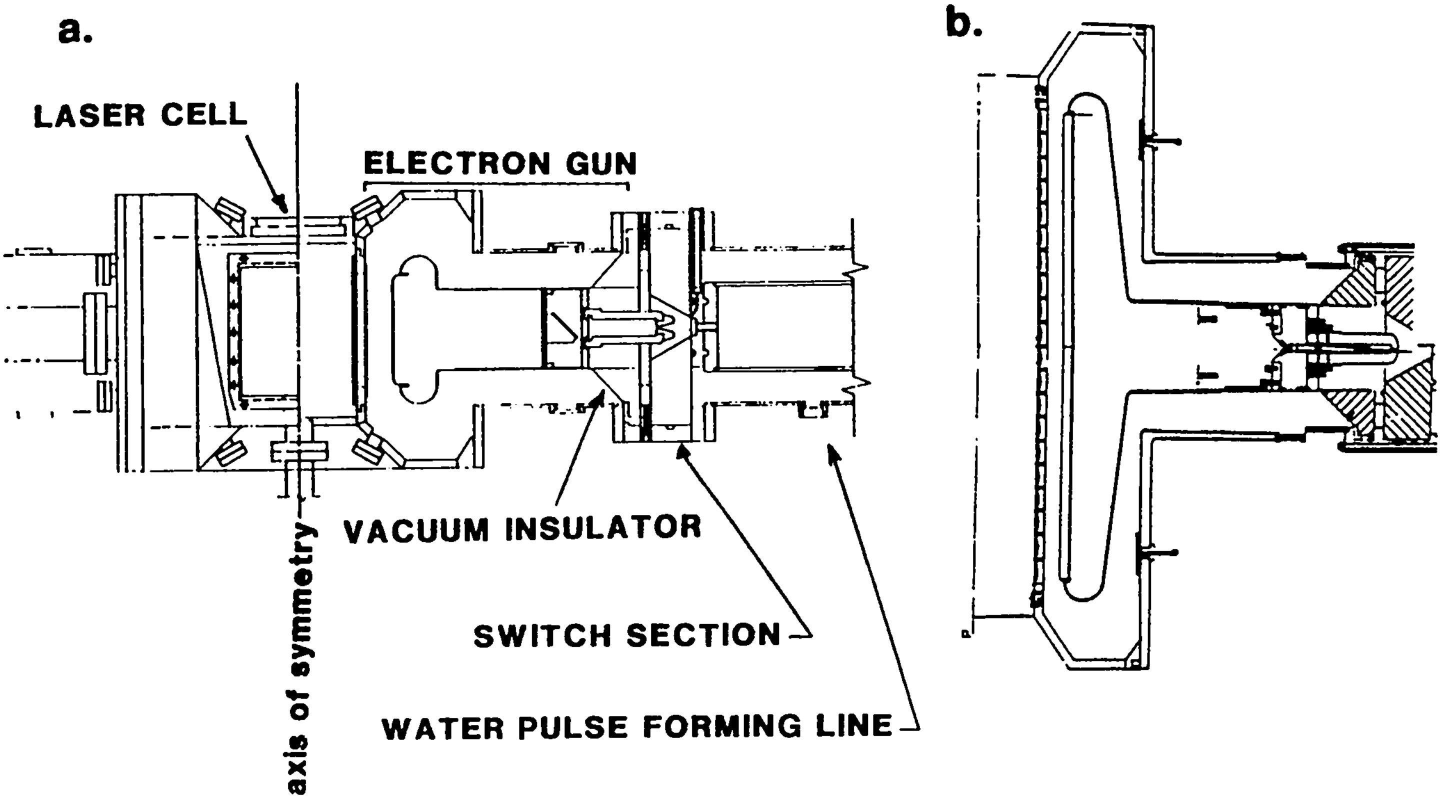

Fig. 1. a. Front view of the 20 cm laser of the NIKE system. b. Top view.

made up of stainless steel rectangular bars 3.2 - mm thick and 1.3 cm deep spaced 2.9 cm apart. The bars are 22 cm tall where they are welded into a frame which provides the vacuum seal to the gun box and supports the gas foil. The open part of the hibachi is larger than the emitter area so all emitted electrons go into the gas. The optical transmission of the hibachi structure alone is 90% . The gas foil is 50 µm of uncoated Kapton. The gun vacuum is routinely less the 5x10-5 torr and up to 1400 torr of gas is used on the other side of the foil in the laser cavity. The pressure on the Kapton causes the foil to bow inward so the distance from the anode screen to the Kapton is 1 cm on average.

The electron beam has been diagnosed by a large sheet of GAF Chromic Dosimetry Media placed inside the laser cell up against the hibachi. One shot was fired with a gun voltage of 240 kV and 1 kG guide field. A gray scale image of the center portion of the beam is shown in Fig. 2. The distribution densitomitered on the media showed a generally uniform distribution with a 30% slope top to bottom due to a error in the anode-cathode (AK) spacing. The size of the beam was only slightly larger than the emitter area ($21 \times 81\ \mathrm{cm}^2$ 10% of peak energy density). Assuming a uniform current distribution the geometric shape of the electron beam gives the following self generated magnetic field for near the center on the top and bottom of the beam as well as the field near the center on the ends:

$$B_s(\mathrm{T}) = 0.62 \times I(\mathrm{MA}) \qquad (1)$$

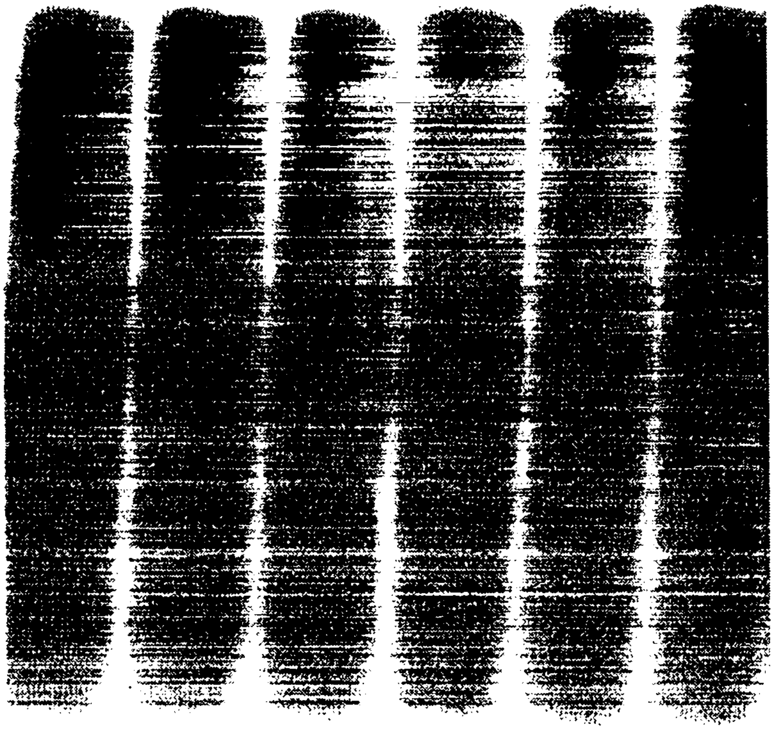

Fig. 2. Gray scale image of the center 20 cm of the electron beam of one electron gun taken just as the electrons emerge into the gas. No regular structure other than the blockage from the hibachi bars is visible. Magnetic field slant effects are visible in the hibachi shadows on the top and bottom.

If there is no guide magnetic field, then an electron emitted from the cathode near the edge will be accelerated through the perpendicular magnetic field. In Child-Langmuir limited current flow[2] the electron's initial velocity is very small, approximately the temperature of the cathode plasma. Since the electron will become nearly relativistic during its travel, a small relativistic correction can be approximated by a correction in ω_c. Defining $+z$ as the direction of acceleration for the electron and $+y$ to be the short dimension of the cathode (up in the experiment) the self field at the top of the electron beam is in the $+x$ direction. The electrons z velocity is approximately

$$\upsilon_z = \frac{E}{B_s}\sin\left(\omega_c' T\right) \quad \text{where } \omega_c' = \frac{qB}{m\left(1+\frac{1}{2}{\frac{\phi}{m_e c^2}}^{\frac{3}{2}}\right)} \qquad (2)$$

and ϕ is the cathode potential and E is the electric field in the anode-cathode gap. The turning point ($uz = 0$) for an electron would beat $z = 2E/B_s\,\omega_c'$. All of the above expressions are only valid in the anode cathode gap. Once the electron goes through the anode screen there is no accelerating electric field. However, it is a good estimate to see if the electron will significantly decelerate in the gap due to the self generated magnetic field. This estimate does not attempt to deal with the radial component of the space charge electric field . The effect of the space charge field is probably not small but very difficult to estimate given the two conducting surfaces. The field will probably reduce the self pinch . A more complete treatment of the beam in the drift region shows it to be marginally stable.[6]

The instability measurements were made with a gun voltage of 205 kV with a 2.8 cm anode cathode gap. The gun is driven by an 180 ns long co-axial water line with a laser triggered switch. The current was 60 kA and the maximum self generated magnetic field is 372 gauss. The turning point is $z = 6.7$ cm, well above the anode-cathode gap. Therefore, according to this simple estimate, at this operating point there should be no real need to apply an external magnetic field to prevent self pinch.

Figure 3 shows a series of voltage traces and integrated current traces for three values of guide magnetic field. In the lowest field case the current trace is distorted and the voltage probe shows high frequency oscillations on the voltage pulse. A B-dot probe was inserted just above the anode-cathode gap approximately 15 cm from center. Figure 4 shows the oscillations for the more sensitive probe. No integrator was used with this probe to retain the high frequency response. The expanded timescale photograph shows the highest frequency to be around 1.5 GHz., however the oscilloscope bandwidth is 1 GHz. and higher frequency components could be filtered out. The amplitude of the instability vs the applied guide magnetic field is shown in Fig. 5. The critical field for the turn on of the instability appears to be very close to the estimated value of the self generated magnetic field. It is not obvious why the electron beam should go unstable at this point.

If a virtual cathode were to develop in the short drift region between the anode screen and the kapton foil\laser gas interface then the electrons would slow down as a beam-plasma instability would develop. The growth rate of the instability can be estimated[7] by

$$\gamma = \frac{\sqrt{3}}{2\frac{4}{3}}\,\delta\frac{1}{3}\,\omega_p \text{ beam} \qquad \delta = \frac{n_e \text{ virt. cath.}}{n_e \text{ beam}} \tag{3}$$

The growth rate will be 1/2 the beam electron plasma frequency when the virtual cathode density is only 12% of the beam density. The seed for the virtual cathode is probably backscatter from the Kapton and laser gas. Kapton transmission of high energy electrons significantly degrades below 160 keV. If the electrons have a significant angle away from normal, then higher energy electrons will be absorbed or backscattered from the Kapton. In particular, as the Kapton absorbs electrons it would become charged, increasing the number of electrons which would reflect.

Fig. 3. Electron gun voltage and integrated current traces for (a.) 400 gauss, (b.)200 gauss, (c.) 0 gauss. The average flat top voltage is 205 kV and the average flattop current is 60 kA. The spike on the voltage trace is a laser trigger fiducial.

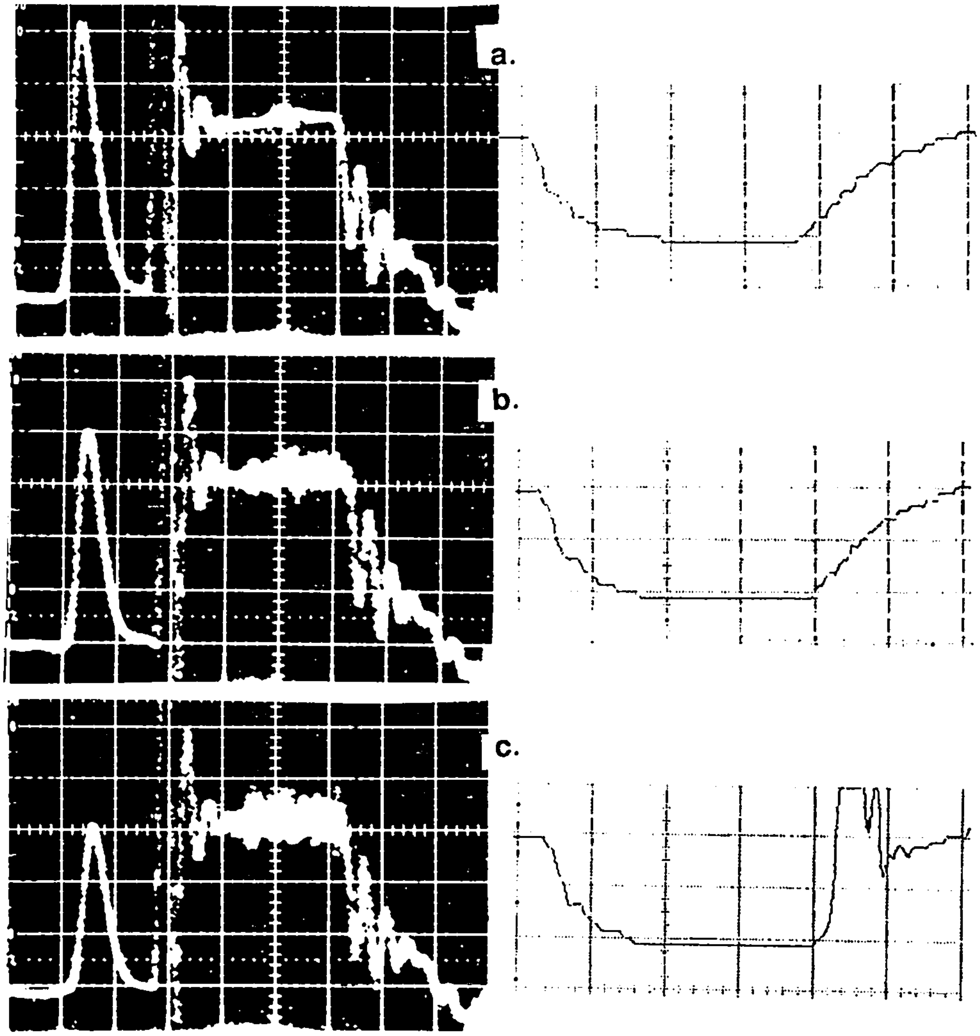

Fig. 4. Unintegrated B-dot current probe located 15 cm from the horizontal and vertical centerline in the A-K gap with a 70 gauss magnetic guide field.

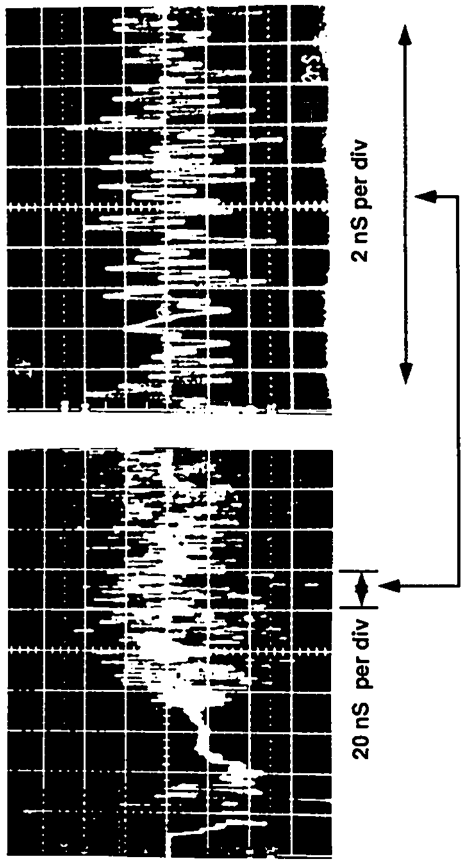

Fig. 5. Amplitude of the oscillations on the B-dot probe as a function of the guide field strength. The oscillation strength varied by 50% for zero guide field.

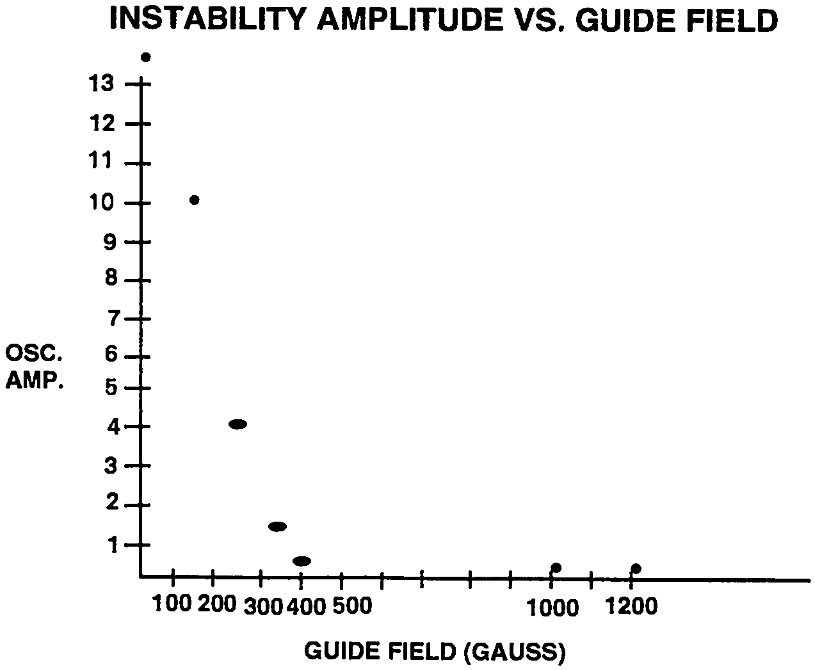

Additional evidence that the instability is occurring in the drift region is obtained from the voltage and current traces prior to onset of the instability. The voltage and currents are virtually unchanged from 0 magnetic field to 1 kG, indicating no significant change in the Child-Langmuir limited flow, hence no significant pinching effect or charge build-up in the anode-cathode gap prior to onset of the instability. The plasma frequency for the beam ($\omega_{p\mathrm{beam}}$) in the vicinity of the anode should be 1 GHz., close to the frequency observed. In order to examine some of these issues quantitatively, computer simulations are required.

III. Simulation Results

One dimensional steady state analysis of electron flow is commonly used to predict behavior of electron beams in real devices. While this approach is successful in many applications where the dynamics are not strictly one dimensional, it cannot be applied to this problem. One approach which can be used is to use a 2-d code and assume a infinitely long cathode. However, as will be described, three dimensional analysis became is more relevant. Simulations using the experimental parameters were performed on the ISIS PIC code at Los Alamos.[8] The code solves the complete set of Maxwell's equations together with a particle in cell treatment of the particle dynamics. The pulsed power is fed into the simulation via a TEM wave on the cathode side of the simulation region. The cathode is treated as a perfect conductor with space charge limited emission. The anode is treated as a lossless conductor of zero thickness.

Simulations have been performed in both two and three dimensions. The two dimensional simulations correspond to the center plane of the three dimensional simulations, the long and thin approximation. The simulations show that there is a virtual cathode instability for some parameters.

The threshold is lowest for long drift spaces and no applied magnetic field. The threshold for the two (three) dimensional simulations with a 2 cm drift space is a voltage of about 270KV (210KV). The threshold for the two (three) dimensional simulations with a 1 cm drift space is about 400KV (320KV). An applied magnetic field comparable to the self magnetic field stabilizes the system. Note that the nominal drift space is 2 cm. However, in actual operation gas pressure forces the foil toward the anode screen to give an effective drift space which is thought to be about 1 cm.

Results from three different simulations are presented in order to elucidate the instability mechanism. The simulations are three dimensional, have approximately 100,000 grid cells, with approximately 100,000 particles. Since the particles are concentrated in a relatively small number of cells, there are many particles per cell in those cells that are occupied. The cathode has an emitting area of 20 cm by 80 cm cm, the AK gap is 2.8 cm, the drift distance is 2.0 cm, the voltage is 300 kV, and the resulting current is approximately 80 kA. The self magnetic field was approximately 0.5 KG for all three cases. The three values of the guide field simulated were (a) 0 KG, (b) 0.125 KG, and (c) 0.25 KG. These values are in the range of the experimental study, although the voltage is somewhat high. Figure 6 shows the magnetic field recorded at a point in the AK gap for cases (a), (b) and (c) and Fig. 7 shows the magnetic field recorded at a point in the drift space for the same cases. Magnetic field oscillations exist at lower magnetic fields, whereas the oscillations are eliminated by using larger guide magnetic fields. The magnitude of the oscillations increases substantially in the drift region. Also evident in Fig. 7 are the presence of low frequency oscillations due to the gross pinching of the electron beam.

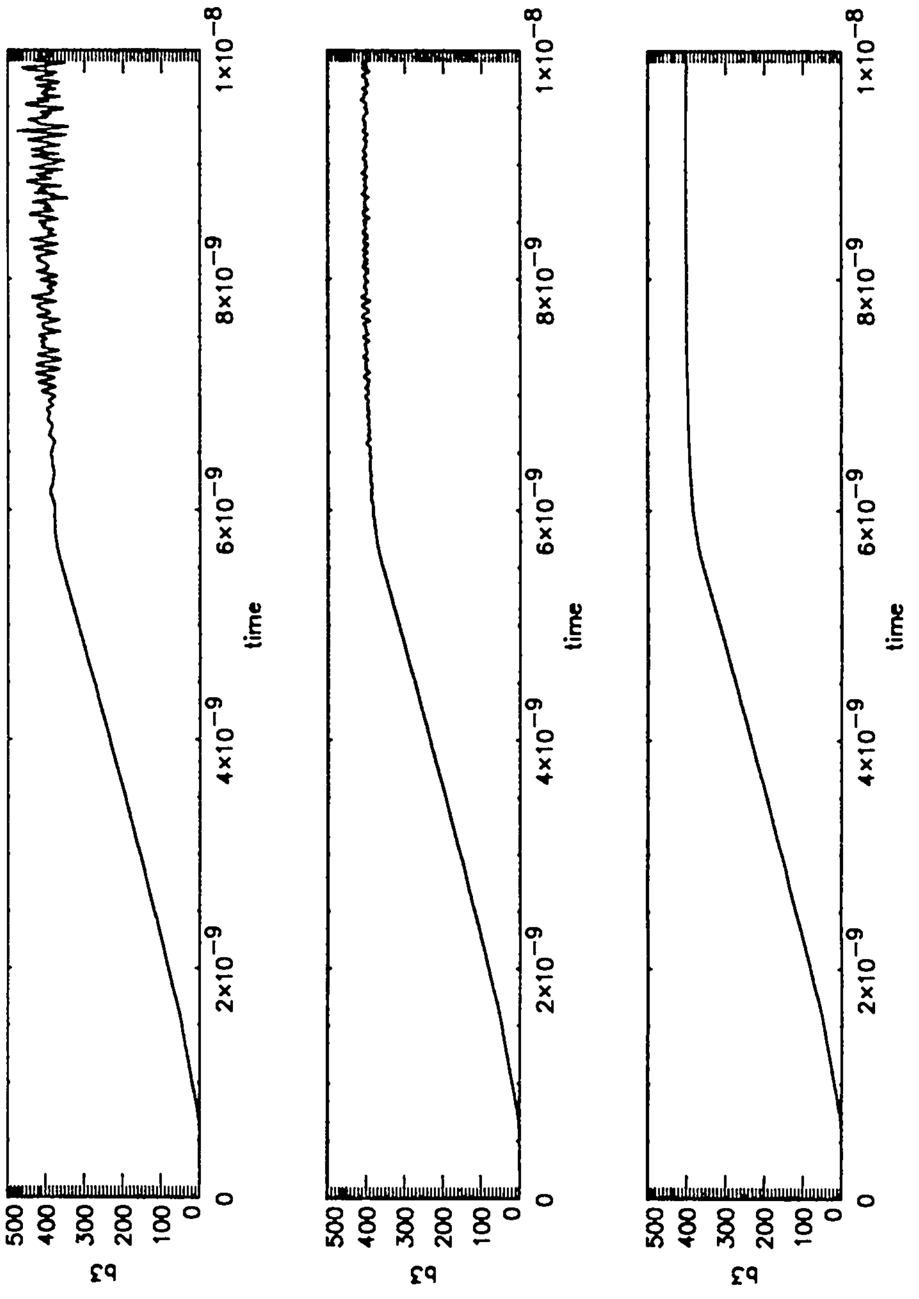

Fig. 6. Traces of the magnetic field in the short direction of the cathode (the "three" direction) inside the AK gap but outside of the beam. The instability in present in parts (a) and (b) but is absent in part (c).

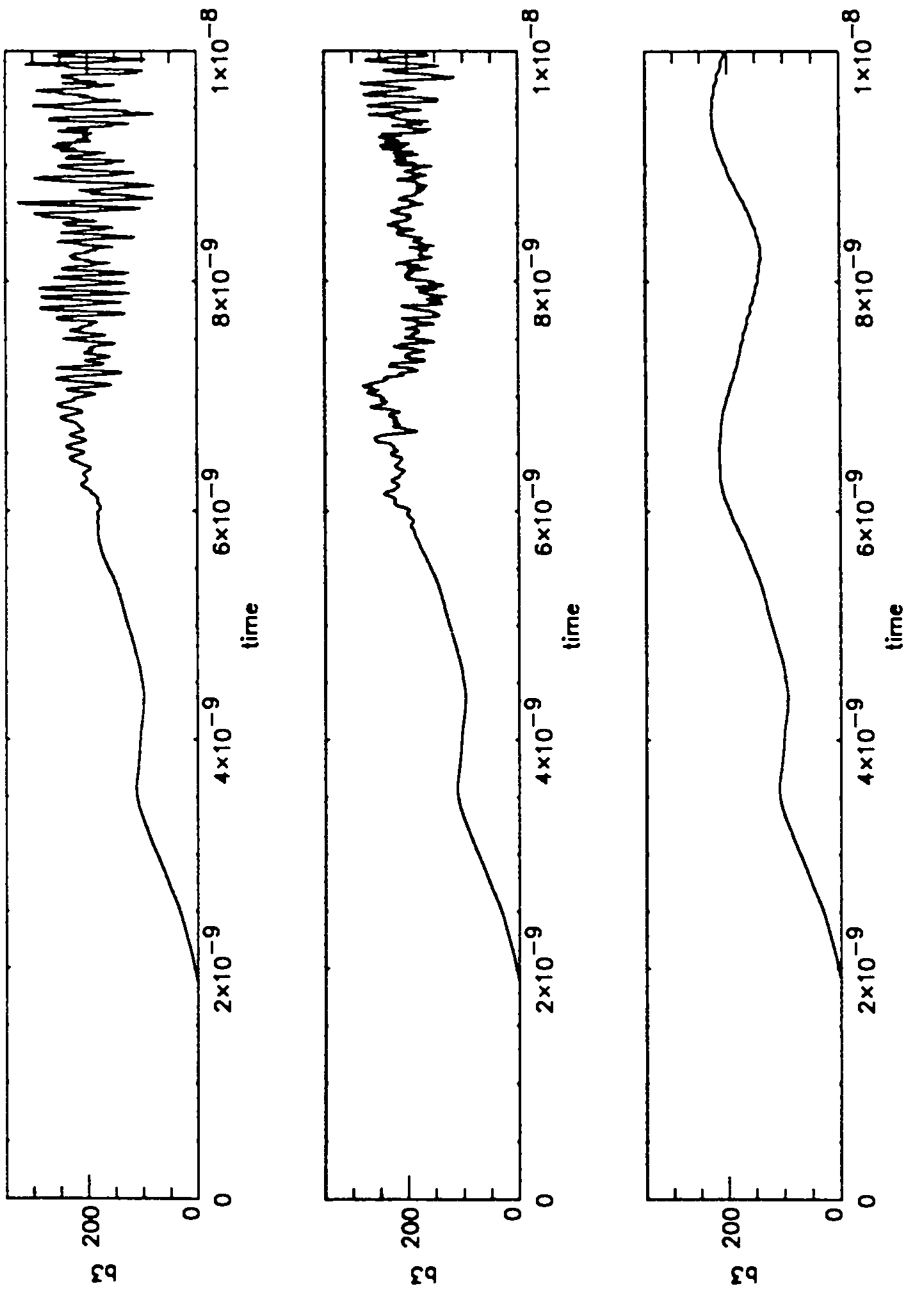

Fig. 7. Traces of the magnetic field in the short direction of the cathode (the "three" direction) inside the drift region but outside of the beam. The instability in present in parts (a) and (b) but is absent in part (c). Notice that the low frequency oscillations persist in even for case (c). These oscillations are due to the beam self pinching, which periodically changes the extent of the beam, thus changing the strength of the magnetic field at the point of observation.

The mechanism for creation of the high frequency oscillations is directly observable from phase space plots of the electrons in the simulations. Figure 8 shows phase space plots of $x1$ vs $p1$ for case (a), (b) and (c). Here $x1$ is the coordinate in the direction of the AK gap and $p1$ is the corresponding momentum (normalized to $m_e c$). There is a significant spread in $p1$ at the anode. This spread in p1 is due to the differential pinching of the electron beam which depends upon the location of the electron in the beam. Those electrons on the outside of the electron beam are pinched more than those on the inside of the electron beam. Moreover, the energy of the electrons at the anode is roughly constant, and so this requires that the electrons undergoing significant transverse pinching motion also have reduced axial momentum. The beam pinching at the edges of the beam serves to increase the local space charge, which further reduces the axial momenta of those particles on the ends on the beam.

This suggests that those electrons involved in the virtual cathode behavior originate primarily on the edges of the beams. This is shown in Fig. 9, which displays p1 vs $x1$ and $x1$ vs $x2$ for case (a). The scatter plot of $x1$ vs $x2$ (Fig. 9b) demonstrates that the electrons that undergo the virtual cathode behavior are indeed located on the edge of the beam. Since the diode is not square, the directions $x2$ and $x3$ are not equivalent and more pinching occurs on the edges of the long dimension of the beam $x2$. This explains why the three dimensional simulations show a lower threshold for beam pinching than the two dimensional simulations. The three dimensional simulations have more space charge on the ends of the beam, since the beam is being pinched in both directions, which in turn slows down those electrons on the end of the beam (near the lower and upper x2 values) more than those in the center of the beam (those near the

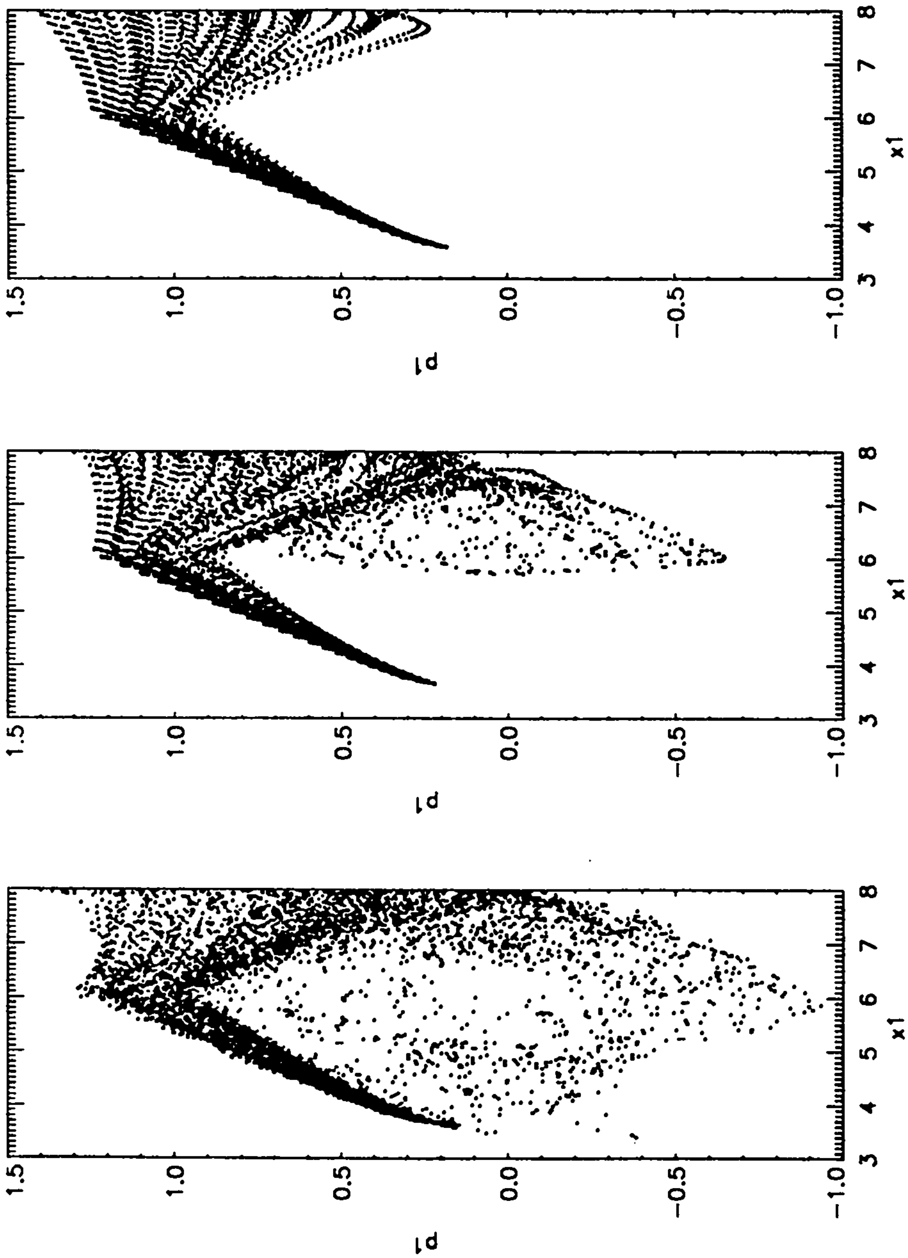

Fig. 8. Phase space plots for cases (a), (b), and (c) corresponding to Fig. 4 which shows p1 (normalized to m_ec) vs x1 integrated over x2 and x3. Only a small percentage of the electrons is shown. Virtual cathode formation is evident in (a) and (b), but not in (c). Note, however, that even in case (c) some electrons barely make it across the drift space and in reality may be reflected from the surface of the foil at the end of the drift space since they impact the foil at a shallow angle of incidence.

mid plane in x2, corresponding to the two dimensional approximation).

Experimental data shows instabilities down to cathode voltages of 205 kV. This discrepancy with the simulations suggest that the actual experimental conditions are lowering the threshold . Two mechanisms which can cause the lower threshold are electrons which are backscattered from the foil and gas and the effect of a net charge build up on the foil. The first mechanism provides the initial trapped electrons in the drift region to augment formation of a virtual cathode. The second mechanism provides an additional repelling force to the electrons further slowing them down in conjunction with the mild pinch on the electron beam . Note that the trajectories in Fig. 8 imply a large angle of incidence for electrons on the edge of the beam in the long (x2) direction. Many of these will be reflected from the foil, serving to lower the voltage required for instability.

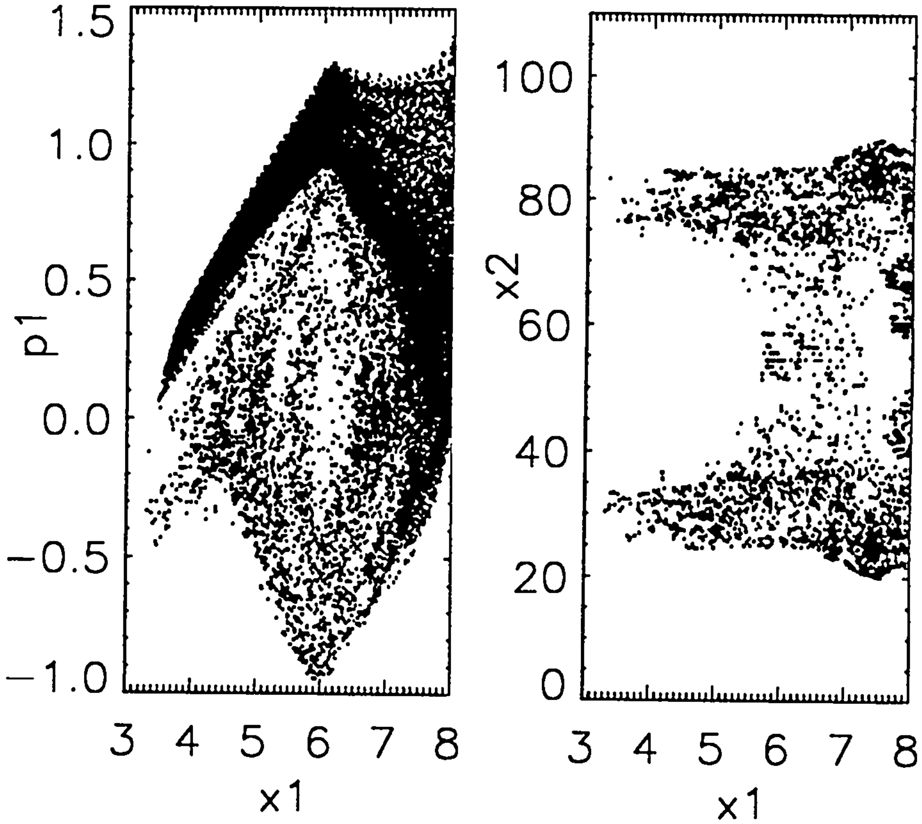

Fig. 9. Phase space plots from case (a) showing (a) p vs x1 and (b) x1 vs x2 for those electrons with negative momentum. More particles are shown than in Fig. 5, however it is still only a small portion of the total number of simulation electrons. The vast majority of electrons with negative momenta are located at the ends of the beam, since it is those electrons that undergo the most pinching.

These mechanisms have been partially examined in the simulations . One severe limitation is the lack of a good backscattering model based on experimental data , particularly when the electrons strike the Kapton and gas surface at an angle over the range of energies in the experiment. A simple two step model dependent on the axial momentum where electrons over the fixed energy are transmitted and those under are reflected led to some results which were close to the experimental data, however the simulations were unstable with minor changes, resulting in so much charge appearing in the drift region a two-stream instability began to turn off the current in the anode-cathode gap.

The foil charging model (neglecting fringing fields) in the three dimensional simulations gave some interesting results. The instability occurred at 200 kV on the gun when there was a 10 kV charge up on the foil and a 2 cm drift region. A 1 cm drift region required an unbelievable 80 kV charge.

More complicated models were examined to combine energy distribution effects with some of the previous models, but did not significantly change the results. The difficulty in obtaining accurate scattering models and properly accounting for the hibachi bars and foil displacement makes a complete calculation unfeasible. Fortunately, the basic mechanism remains the same with all of the scattering and foil charge effects, with only the instability threshold changing.

Self consistent particle simulations have demonstrated that a one dimensional analysis of a pinched electron diode is not adequate. In particular, the maximum drift region for which the beam can be transported without virtual cathode formation can be greatly reduced when the electron trajectories have curvature. The pinching effect and seed terms for the virtual cathode formation are removed when the applied guide magnetic field becomes strong enough so that the experiment can begin to be a one dimensional problem.

Simulations also indicate the presence of another instability when the impedance of the diode is reduced below about two Ohms. In this case the entire beam is scattered, not just the edges of the beam. Unlike the instability described in this paper, the instability occurs in the AK gap, and not primarily in the drift region. Furthermore, an imposed magnetic field comparable to the self magnetic field is not sufficient to eliminate the instability. The low frequency oscillations seen in Fig. 7 may be related to the onset of this low impedance instability. Experimental evidence for these instability was obtained[9] from the Large Aperture Module portion of the AURORA laser system.[4] This diode operated at approximately 1.5 Ohms. Experimental results indicate substantial scattering in the energy of the electron beam.

IV. Summary

The experimental data from the NRL Nike 20 cm amplifier in the case of a relatively low voltage electron gun shows how a problem which would normally be discounted from a one dimensional analysis can become extremely important. Drift regions in large area electron guns must be carefully analyzed with particular attention to inevitable backscattered electrons and actual electron trajectories in this region. Three dimensional simulations are useful in examining possible problems which are not readily recognizable from simple estimates. Experimental data for higher gun voltages is not available as the instability causes arcs in the gun structure that damage the machine. The available data provides a point check on the code which then could be extended to other operating parameters.

V. Acknowledgement

This work was·done in collaboration with C. J. Pawley. T. Lehecka, S. P. Obenschain, and J. Bone, of the Naval Research Laboratory.

"Neutron Time-of-Flight Ion Temperature Diagnostic for Inertial Confinement Fusion Experiments"

References

1. R. A. Lerche and B. A. Remington, Rev. Scient. Instr. **61**, 3131 (1990).
2. M. D. Cable, J. Appl. Phys. **60**, 3068 (1986).
3. H. Brysk, Plasma Physics **15**, 611 (1973).
4. R. A. Lerche, S. P. Hatchett, M. D. Cable, M. B. Nelson, and T. J. Murphy, "Plasma Temperatures from First-Hit Neutron Time-of-Flight Spectra," in 9th Topical Conference on High Temperature Plasma Diagnostics (Santa Fe, NM, these proceedings), March 1992.
5. G. F. Knoll, *Radiation Detection and Measurements*, 2nd edition, Wiley, 1989, Table 8-3.
6. Richard Madey, Frank M. Waterman, Alan R. Baldwin, James N. Knudson, J. D. Carlson, and J. Rapaport, Nucl. Instrum. Meth. **151**, 445 (1978).
7. B. Turko, R. C. Smith, "A Precision Timing Discriminator for High Density Detector Systems," LBL-30602."

Radiation Field Effects on the Spectroscopic Properties of C1 and Fe Seeded Plasmas

1. A. H. Gabriel and C. Jordan, Case Studies in Atomic Collision Physics II, 211 (1972).
2. R. Mewe and J. Schrijver, Astron. Astrophys., **65**, 99 (1978).
3. M. H. Key and R. J. Hutcheon, Advances in Atomic and Molecular Physics, **16**, 201 (1980).
4. C. DeMichelis and M. Mattioli, Nuclear Fusion, **21**, 677 (1981).
5. T. F. Stratton, Plasma Diagnostic Techniques R. H. Huddlestone and L. L. Leonard, eds., Academic Press, New York, 12965, p. 359).
6. R. W. Lee, B. L. Whitten, and R. E. Stout, J. Quant. Spectrosc. Radiat. Transfer, **32**, 91 (1984).
7. J. Abdallah, Jr., R. E. H. Clark, and J. M. Peek, Phys. Rev. A, **45**, 3980 (1992).
8. R. W. Lee, "User Manual for Ration," Lawrence Livermore National Laboratory report, 1990.
9. R. D. Cowan, "Theory of Atomic Spectra" (University of California Press, Berkeley, CA, 1981).

10. J. Abdallah, Jr., R. E. H. Clark, and R. D. Cowan, Los Alamos Manual No. LA-11436-M-I, unpublished data, 1988.

11. R. E. H. Clark, J. Abdallah, Jr., G. Csanak, J. B. Mann, and R. D. Cowan, Los Alamos Manual, LA-11436-M-II, unpublished data, 1988.

12. R. E. H. Clark, J. Abdallah, Jr., and J. B. Mann, Astrophys J., 381, 597 (1991).

13. J. F. Seely, Atomic Data Nuclear Data Tables, **26**, 137 (1981).

Amplified Spontaneous Emission Produced by Large KrF Amplifiers

1. J. J. Tiee, C. R. Quick, A. H. Hsu, and D. E. Hof, Physica Scripta **41**, 71 (1990).
2. Tamagake and D. W. Setser, J. Chem. Phys. **67**, 4370 (1977).
3. H. Pummer, K. Hohda, and F. Rebentrost, Appl. Phys. **20**, 129-134 (1979).
4. Joel Tellingheusen, A. K. Hays, J. M. Hoffman, and G. C. Tisone, J. Chem. Phys. **65**, 4473 (1976).
5. C. W. Patterson and D. E. Hanson, LANL memo dated April 7, 1989.
6. J. R. Murray and H. T. Powell, J. Appl. Phys. **54**, 4275 (1983).
7. P. Jeffrey Hay and Thom H. Dunning, Jr., J. Chem. Phys. **66**, 1306 (1977).
8. R. Burnham and S. K. Searles, J. Chem. Phys. **67**, 5967 (1978).
9. J. G. Eden, R. W. Waynant, S. K. Searles, and R. Burnham, Appl. Phys. Lett. **733**, (1978).
10. C. Patterson and D. Hanson, LANL memo dated May 12, 1989.
11. Andy McCown, LANL memo dated September 12, 1989.
12. W. L. Morgan, N.W. Winter, and K. C. Kulander, J. Appl. Phys. **54**, 4275 (1983).
13. Thom H. Dunning, Jr., and P. Jeffrey Hay, J. Chem. Phys. **69**, 134 (1978).
14. S. Szatmari and F. P. Schafer, Appl. Phys. **13**, 33-219, (1984).
15. A. J. Taylor, R. B. Gibson, and J. P. Roberts, Appl. Phys. Lett. **52**, 773-775 (1988).
16. P. H. Bucksbaum, J. Baker, R. H. Storz, and J. C. White, Optics Lett. **7**, 399 (1982).
17. J. Banic, T. Efthimiopoulas, and B. P. Stoicheff, Appl. Phys. Lett. **37**, 686 (1980).
18. L. M. Frantz and J. S. Nodvik, J. Appl. Phys. **34**, 2346 (1963).
19. S. Szatmari and F. P. Schafer, J. Opt. Soc. Am. B, Vol. 4, 1943-1948 (1987).
20. P. W. Milonni, R. B. Gibson, and A. J. Taylor, Opt. Soc. of Am. B, 5-1360 (1988).
21. J. A. Mangano, J. H. Jacob, M. Rokni, and A. Hawryluk, Appl. Phys. Lett. **31**, 26-28 (1977).
22. A. M. Hawryluk, J. A. Mangano, and J. H. Jacob, Appl. Phys. Lett. **31**, 164-166 (1977).
23. S. Thomas, L. Lopez, and K. Hosack, "Private Communication", January 1989.
24. J. A. Oertel, S. J. Czuchlewski, W. T. Leland, T. P. Turner. Paper presented at CLEO 90.
25. Chemical and Laser Science Division Annual Report 1990, LA-12107-PR, pp 18-19.
26. S. Czuchlewski, "LANL Private Communication".
27. LANL internal report, "Prepulse Target ASE in Aurora", W. T. Leland, February 5, 1990.
28. LANL internal report, "Aurora Phase/Prepulse Calculation," May 10, 1991.
29. R. Kristal, LANL "Private Communication".

1. A. H. Gabriel and C. Jordan, Case Studies in Atomic Collision Physics II, 211 (1972).
2. R. Mewe and J. Schrijver, Astron. Astrophys., **65**, 99 (1978).
3. M. H. Key and R. J. Hutcheon, Advances in Atomic and Molecular Physics, **16**, 201 (1980).
4. C. DeMichelis and M. Mattioli, Nuclear Fusion, **21**, 677 (1981).
5. T. F. Stratton, Plasma Diagnostic Techniques R. H. Huddlestone and L. L. Leonard, eds., Academic Press, New York, 12965, p. 359).
6. R. W. Lee, B. L. Whitten, and R. E. Stout, J. Quant. Spectrosc. Radiat. Transfer, **32, 91** (1984).
7. J. Abdallah, Jr., R. E. H. Clark, and J. M. Peek, Phys. Rev. A, **45**, 3980 (1992).
8. R. W. Lee, "User Manual for Ration," Lawrence Livermore National Laboratory report, 1990.
9. R. D. Cowan, "Theory of Atomic Spectra" (University of California Press, Berkeley, CA, 1981).
10. J. Abdallah, Jr., R. E. H. Clark, and R. D. Cowan, Los Alamos Manual No. LA-11436-M-I, unpublisheddata, 1988.
11. R. E. H. Clark, J. Abdallah, Jr., G. Csanak, J. B. Mann, and R. D. Cowan, Los Alamos Manual, LA-11436-M-II, unpublished data, 1988.
12. R. E. H. Clark, J. Abdallah, Jr., and J. B. Mann, Astrophys J., 381, 597 (1991).
13. J. F. Seely, Atomic Data Nuclear Data Tables, **26**, 137 (1981).

FOR FURTHER INFORMATION, CONTACT:

Stephen M. Younger
Program Director, ADNWT/ICF
MS E527
Los Alamos National Laboratory
Los Alamos, NM 87532
(505) 667-5167

This document was produced on a Macintosh II™, Varityper VT600P™, and Cannon™ Scanner using Microsoft Word™, Expressionist™, Adobe Illustrator™, and Pagemaker™.

Compiled, edited, and produced by Liz Courtney.

LALP-93-30
January 1993